Measurement of the b-jet cross section at $\sqrt{s}$ =1.96 TeV

O. Peters

February 6, 2003

Contents

Chapter 1

Triggers used for data selection

The measurement of the b-jet cross section with a muon tag requires the presence of both a reconstructed muon and a jet in the event. A trigger that requires both a muon and a jet will therefore give the highest purity at the highest rate. Single muon or jet triggers give a lower purity, and due to the fact that they ran prescaled in the triggers used, they also give a lower rate.

At the time of data taking, only a part of the Level 1 Trigger System was working reliably enough to select muons and jets. Level 2 and Level 3 were running in Mark & Pass mode, which means that every event that was triggered by Level 1 passed both Level 2 and Level 3. The Level 1 Trigger System included the calorimeter trigger in the $|\eta| < 0.8$ region, as well as the muon scintillator trigger, albeit without the matching of tracks from the CTT. Therefore, the trigger used to select the data requires:

- An A+C scintillator coincidence in the muon detector with $|\eta| < 2.0$, with no requirement on the presence of a central track in the CTT;
- A 5 GeV energy deposit in the calorimeter with $|\eta| < 0.8$.

This trigger is combined under the name $mu1ptxatxx\_CJT5$, where the first part, $mu1ptxatxx$, corresponds to the muon part while the second part, $CJT5$ refers to the calorimeter part of the trigger.

1.1 Efficiency for Jet+μ Trigger

To calculate the efficiency of this trigger, we split it in two parts: the Level 1 muon trigger efficiency, ϵ^{μ}_{L1}, and the Level 1 calorimeter trigger efficiency, ϵ^{cal}_{L1}, and we calculate both efficiencies separately. If we ignore the correlation between those two triggers for now, we can state for the combined Level 1 efficiency:

$$\epsilon_{L1} = \epsilon^{\mu}_{L1} \cdot \epsilon^{cal}_{L1} \tag{1.1}$$

Correlations between the jet and muon trigger efficiency may occur due to two effects:

- Punch-through of particles in a jet into the muon system, faking a muon and firing the muon trigger;
- Energy deposits by a real muon in the calorimeter that biases the jet trigger.

In section 1.1.3 we will discuss these effects, which turn out to be small.

The strategy to measure ϵ_{L1}^{μ} and ϵ_{L1}^{cal} is based on the use of independent reference triggers. Events that are triggered by these reference triggers are fully reconstructed. In the case that a jet or muon is present, it is checked if the corresponding trigger bit is set. This allows the calculation of the trigger efficiency, as explained in the following sections.

1.1.1 Level 1 Calorimeter Trigger Efficiency

The calorimeter trigger efficiency for the CJT5 trigger used is calculated by selecting events from the initial data that are triggered by a muon trigger, akin to the $mu1ptxatxx$ trigger explained above, with the additional requirement of a hit coincidence in the luminosity counters, which signals the presence of a hard scattering. In addition, the presence of a reconstructed jet passing quality and kinematic cuts (see section 3) is required. The CJT5 trigger efficiency is calculated by selecting the events in which the $mu1ptxatxx\_CJT5$ trigger fired, divided by the number of events in the selected sample, viz.

$$\epsilon_{L1}^{cal} = \frac{Reconstructed\ jet\ and\ mu1ptxatxx\_CJT5\ set}{Reconstructed\ jet\ and\ mu1ptxatxx\ set} \tag{1.2}$$

Figure 1.1a shows the efficiency of the CJT5 trigger as a function of reconstructed jet E_T (uncorrected), η and ϕ. Correcting the jet energy with the Jet Energy Scale results in figure 1.1b. The statistical errors on the trigger efficiency are shown as the vertical lines on the data points.

The systematic error is calculated from the uncertainty on the Jet Energy Scale correction, which is of the order of 7%. First, the error on the Jet Energy Scale correction is added to the correction for each separate jet, and the Level 1 efficiency is calculated. Then, the same is done but by subtracting the error on the Jet Energy Scale correction. The maximum difference of these two efficiencies with respect to the efficiency calculated with no error on the Jet Energy Scale correction is taken as the systematic error, which is illustrated by the gray band on the bottom of figure 1.1b.

The Level 1 trigger efficiency shows a turn-on curve for jet energies below 40 GeV, reaching a 100% efficiency above that energy.

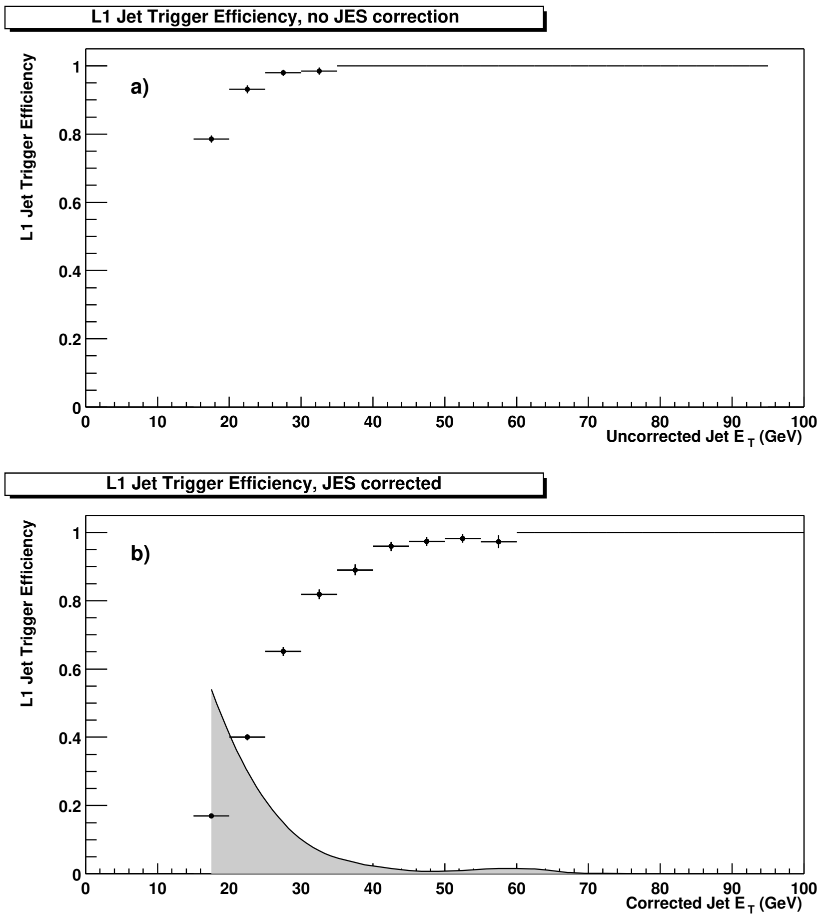

Figure 1.1: *Level 1 Jet Trigger efficiency, uncorrected (top) and corrected (bottom) for the Jet Energy Scale. Data points show statistical error with the gray band showing the relative systematic error.*

1.1.2 Level 1 Muon Trigger efficiency

The Level 1 muon trigger requires a coincidence of a scintillator hit in the A-layer and a scintillator hit in the B- or C-layer. Two reference triggers, which both contain the CJT5 And-Or Input Term, are used to calculate the efficiency of this trigger, namely:

- $2JT\_LO$, requiring two Level 1 calorimeter towers with $E_T > 3$ GeV and one with $E_T > 5$ GeV. In addition, at Level 3, two jets reconstructed with a simple cone algorithm and with $E_T > 10$ GeV are required;
- $CEM5\_2CJT5$, requiring two Level 1 calorimeter towers with $E_T > 5$ GeV, in addition to a 5 GeV energy deposit in the electromagnetic calorimeter.

For each of these triggers, a sub-sample is extracted from the initial sample for which the reference trigger fired, and an offline reconstructed tight muon that passed modified quality and kinematic cuts was present in the event. These modified quality cuts are the same ones used as described in section 3.1, but with the scintillator hit requirement on the muon tracks removed. This is done to avoid the bias introduced by the fact that the standard quality cuts require both an A- and a B- or C-layer scintillator hit, which is the same requirement that fires the trigger if the times measured on the hits are within the trigger gates.

Normally, the presence of a reconstructed jet close to the muon cuts out all cosmic muons. However, the sample that is extracted here does not have that requirement and therefore still contains cosmic muons. The percentage of present muons that are actually cosmic muons is estimated using two methods: using scintillator times associated with the muon track, and back-to-back muons. The first method selects all muon tracks in the sample that have one or more scintillator hits associated with them. The percentage of these tracks that have a measured time on one of the scintillator hits that is outside the trigger gate is taken as the cosmic muon contamination in the sample. This method results in a cosmic contamination of $6.3 \pm 0.6\%$. The second method counts the number of back-to-back muons in the sample, which gives the cosmic muon contamination when divided by the total number of tight muons in the sample. In this scenario a back-to-back muon is defined by a tight muon in the muon system, with another muon at $\delta\phi > 2.5$, at least 2 wire hits in the A-layer and at least 3 hits in the BC-layer of the muon system. This results in a cosmic muon contamination of $2.8 \pm 0.4\%$. To get a proper estimate of the total cosmic muon contamination, these two numbers are averaged, with a systematic error covering the extremities: $4.5 \pm 1.8\%$.

The efficiency of the $mu1ptxatxx$ trigger is now calculated by selecting the events in which the $mu1ptxatxx\_CJT5$ trigger fired, divided by the number of events which contain a reconstructed muon in the selected sample:

$$\epsilon^{\mu}_{L1} = \frac{Reconstructed\ muon\ and\ mu1ptxatxx\_CJT5\ set}{Reconstructed\ muon\ and\ CJT5\ set} \tag{1.3}$$

Reference trigger	Efficiency	Statistical Error
$2JT\_LO$	57.8%	1.5%
$CEM5\_2CJT5$	60.7%	1.4%
Combined	58.1%	1.0%

Table 1.1: *Level 1 muon trigger efficiencies measured with different reference triggers.*

Figure 1.2 shows the Level 1 muon trigger efficiency as a function of p_T, η and ϕ of the reconstructed muon for the $2JT\_LO$ trigger on the left hand side of the plot, and for the $CEM5\_2CJT5$ trigger on the right hand side. The trigger shows a drop in efficiency for high p_T muons. This is not due to a physics or hardware effect but is shown with later runs using more statistics to be a statistical effect. For the later calculation of the μ+jet cross section this effect is taken into account. The drop of efficiency seen in the plot for the Level 1 η efficiency for reference trigger 1 between $0.1 < \eta < 0.5$ can also be attributed to statistics, since this effect is not seen for the second reference trigger. Both the ϕ plots show the effect of hole in the bottom of the detector at $4.2 < \phi < 5.0$, where few muons are found.

Combining the two data samples, taking into account those events for which both reference triggers fired, results in the final L1 muon efficiency as shown in figure 1.3. The average efficiency of the L1 muon trigger is $58^{+2.4}_{-2.7}\%$, where the errors consist of:

- The statistical error of 1.03%;
- The difference between the combined L1 trigger efficiency and the efficiency of the reference trigger (+1.2%, -1.7%);
- An error of 1.8% for the cosmic muon contamination.

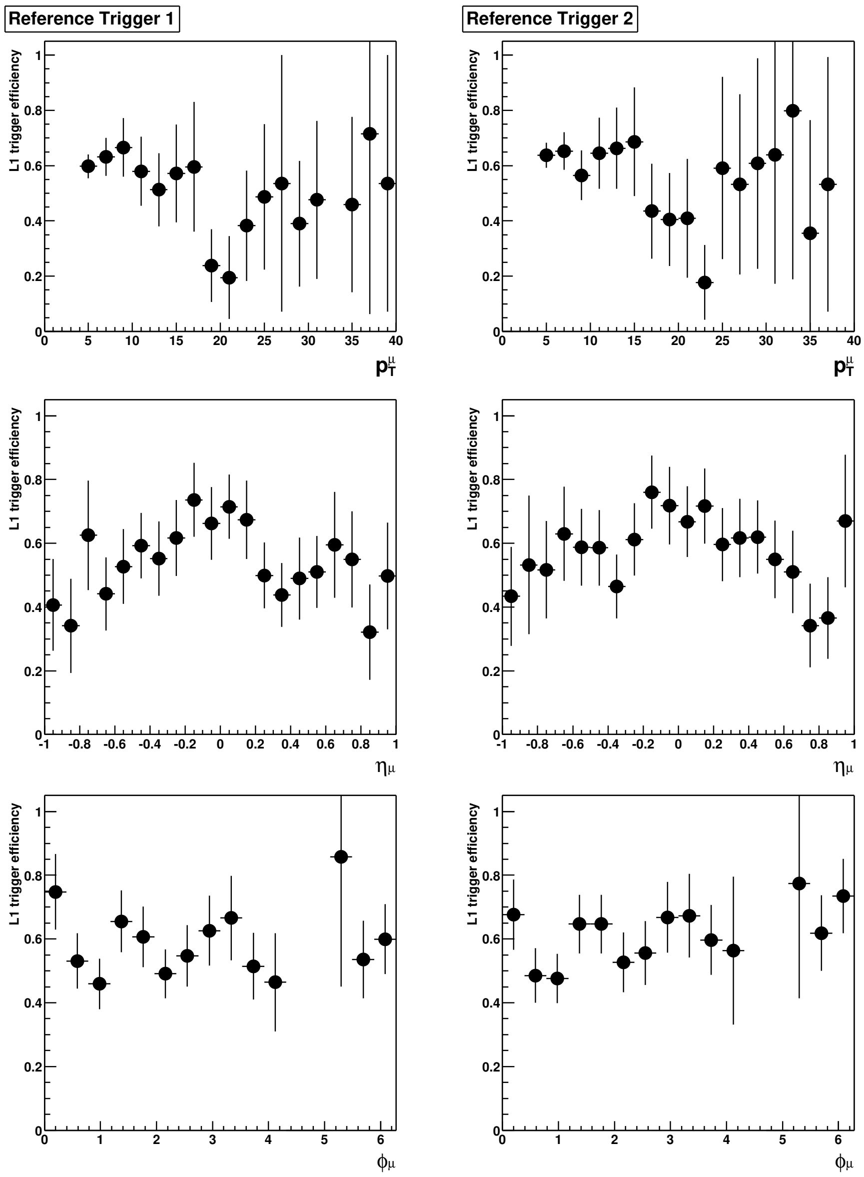

Figure 1.2: *Level 1 muon trigger efficiency as a function of p_T, η and ϕ, for the $2JT\_LO$ reference trigger in the left plots and for the $CEM5\_2CJT5$ reference trigger in the right plots.*

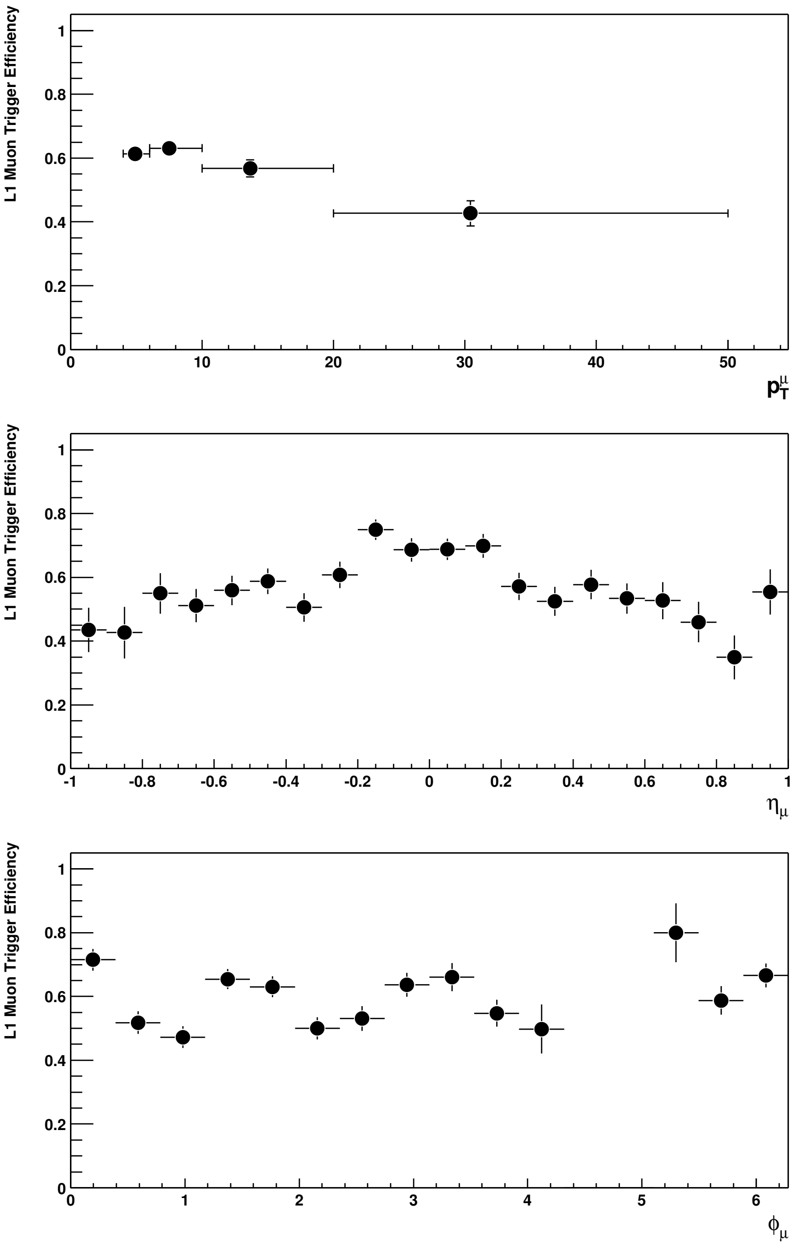

Figure 1.3: *Level 1 muon trigger efficiency as a function of p_T, η and ϕ, using both reference triggers*

1.1.3 Trigger correlations

Equation 1.1 is only valid if the correlation between the two separate triggers is zero. A priori this is not immediately clear: particles in a jet that fires the jet trigger can punch through the calorimeter, firing the muon trigger as well. Also, a muon, firing the muon trigger, could possibly deposit enough energy in the calorimeter to fire the jet trigger.

The correlation of the muon trigger with the jet trigger due to punch-through particles is zero by definition. The denominator in the efficiency calculation for the muon trigger is a muon with at least two wire hits in the A-layer, and at least three wire hits in the BC-layer. Any punch-through particle that creates such a track is indistinguishable from a real muon, and is treated as a real muon in the trigger efficiency measurements. Only at a later stage is the cross section corrected for the effects of punch-through.

A muon passing through the calorimeter will fire the jet trigger if the muon deposits more than 5 GeV in one trigger tower (0.2×0.2 in $\delta\eta \times \delta\phi$-space). The extent of this effect on the jet trigger efficiency is investigated in two ways:

- By determining the energy a muon deposits in the calorimeter;
- By calculating the jet trigger efficiency, in the case that a muon is present in the event.

The energy deposited by a muon in the calorimeter is measured by looking at the energy in the calorimeter in a tower of 3 by 3 cells around an isolated muon track. This 3 by 3 tower is 2.25 times as big as the trigger tower, which causes an overestimation of the energy deposited in a trigger tower. The energy deposited by the muon in a 3 by 3 tower is shown in figure 1.4. The number of entries above the 5 GeV trigger cut-off is $0.23 \pm 0.03\%$ of the total number of entries, which means that the energy deposit of the muon will not fire the trigger by itself. However, it can still bias the jet trigger if this energy deposit is close to a jet. To exclude any possible effect, we also study the jet trigger efficiency in a sample of jets in which a reconstructed muon is present. No significant deviation from figure 1.1 is observed, and we conclude that there is no correlation between the Level 1 muon trigger and the Level 1 jet trigger.

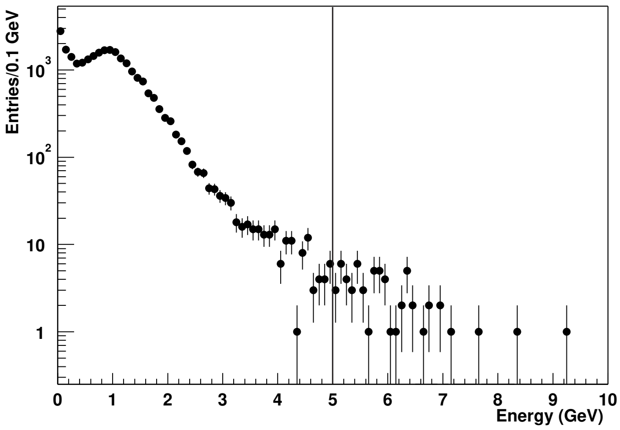

Figure 1.4: *Energy deposition in the calorimeter in a 3x3 tower around an isolated muon track. The vertical line represents the energy above which the Level 1 calorimeter trigger fires.*

Chapter 2

Offline Event Reconstruction

2.1 Jet Reconstruction

The jet reconstruction requires a tower with $E_T > 0.5$ GeV to serve as a starting point from which the jet precluster is formed. This precluster itself is required to have $E_T > 1$ GeV. Absence of such a tower with $E_T > 0.5$ GeV or precluster with $E_T > 1$ GeV will cause the energy that is deposited in the calorimeter not to be assembled into a jet, resulting in an inefficiency. To investigate this possible inefficiency, we study the distributions of transverse energies of towers and preclusters which are used to seed jets. To calculate the inefficiency resulting from not finding the tower, a fit is applied to the distribution of the energy of the highest energy tower in the jet cone, at different energy ranges. The efficiency to find the 0.5 GeV tower in a particular energy range can then be expressed as:

$$Efficiency = \frac{Area\ under\ fit\ above\ 0.5\ GeV}{Total\ area\ under\ fit} \tag{2.1}$$

In other words, the efficiency is the probability for a jet of a given E_T to contain a tower above 0.5 GeV. The energy distributions for two jet energy ranges are shown in figure 2.1. Note, that with increasing jet energy, the tower energy distribution shifts up, and the 0.5 GeV cut does not cut into the fit on the distribution anymore. This yields a 100% efficiency for jets above 20 GeV.

The inefficiency resulting from not finding a precluster with $E_T > 1$ GeV is found in a similar manner, resulting in the distributions shown in figure 2.2 for the same two energy ranges. The seed energy shifts up with increasing jet transverse energy, also yielding an efficiency close to 100% for jets above 20 GeV.

Jets in the Monte Carlo simulation show a similar behavior as jets in the data.

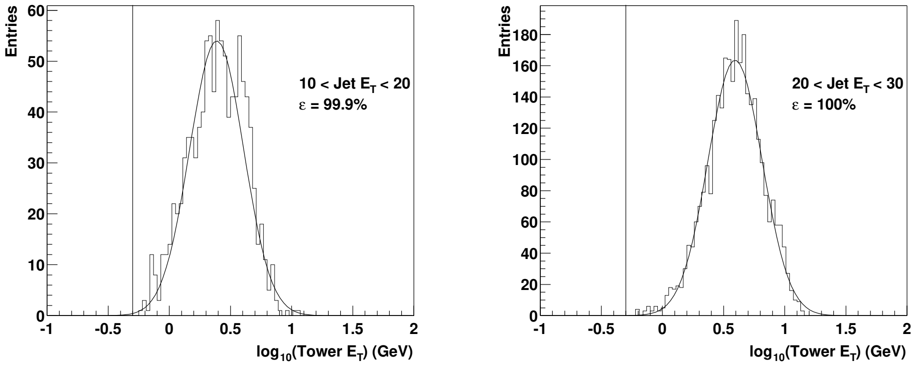

Figure 2.1: *Tower transverse energy distributions for jet transverse energies between 10 and 20 GeV (left) and between 20 and 30 GeV (right). The vertical line represents the 0.5 GeV cut on the tower transverse energy, as it is used in the reconstruction algorithm.*

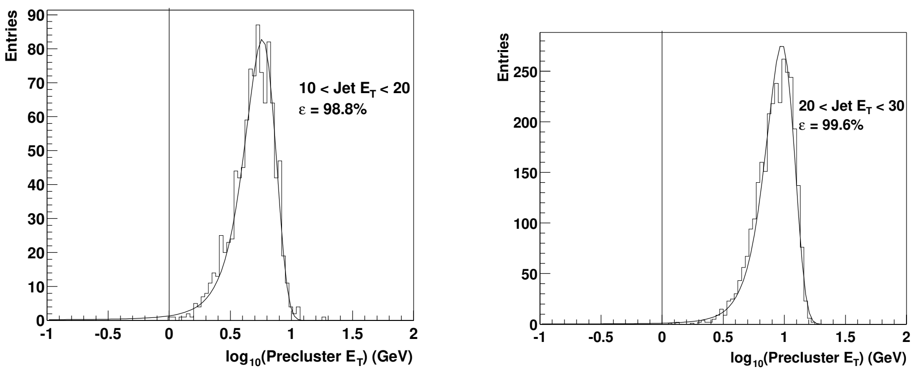

Figure 2.2: *Precluster transverse energy distributions for jet transverse energies between 10 and 20 GeV (left) and between 20 and 30 GeV (right). The vertical line represents the 1 GeV cut on the precluster transverse energy, as it is used in the reconstruction algorithm.*

2.1.1 Jet Energy Resolution

The resolution of Jet Energy Scale corrected jets is extracted from di-jet events using the asymmetry variable $\mathcal{A}$, which is defined as:

$$\mathcal{A} = \frac{p_T^{(1)} - p_T^{(2)}}{p_T^{(1)} + p_T^{(2)}} \tag{2.2}$$

where $p_T^{(1),(2)}$ is the p_T of each jet in the event. When plotted in different bins of p_T^{event}, where

$$p_T^{event} = \frac{p_T^{(1)} + p_T^{(2)}}{2} \tag{2.3}$$

the distribution of this asymmetry variable expresses a gaussian shape with width $\sigma_{\mathcal{A}}$ for $p_T^{event} > 30$ GeV/c. The relative resolution of reconstructed jets, $\frac{\sigma_{p_T}}{p_T}$ can now be expressed as:

$$\frac{\sigma_{p_T}}{p_T} = \sqrt{2}\sigma_{\mathcal{A}} \tag{2.4}$$

For events with low values of p_T^{event}, $p_T^{event} < 30$ GeV/c, the resolution cannot be extracted from the data in this fashion. This is due to the fact that the jet reconstruction only reconstructs jets with uncorrected $E_T > 8$ GeV. The Jet Energy Scale correction of approximately 1.8 for low energy jets scales this lower bound up to 14.4 GeV. Therefore, there is no contribution of jets with $E_T < 14.4$ GeV to the resolution. Jets can fluctuate out of the low E_T bins, but due to the lower bound cut-off, no jets can fluctuate into the low E_T bins. This situation is different in the Monte Carlo simulation, where the Jet Energy Scale correction is approximately 1.2, and the lower bound is scaled up to 9.6 GeV. To avoid biases resulting from this effect, events with $p_T^{event} < 30$ GeV/c are not taken into account in the fit for the jet resolution function.

To measure the asymmetry variable, di-jet events are selected in which both jets pass the standard jet quality cuts (see section 3.2), and with the requirement that:

- Both jets have $|\eta| < 0.6$, the same region in which the cross section is later measured;
- The jets are back-to-back to ensure energy balance in the event: $\Delta\phi > 175°$.

In addition, a number of event quality cuts are imposed on the event:

- A cut on missing E_T : $\not{E}_T < 0.7 p_T^{leading\ jet}$, to ensure reasonable energy balance in the event;
- A cut on the total energy deposited in the calorimeter: $E_{tot} < 2$ TeV, to remove events with noisy calorimeter readout.

The resulting distributions for the asymmetry variable are shown in figure 2.3 for different bins of p_T^{event}. The first two plots, 2.3a and 2.3b, show the effects of the low energy cut-off in the data. Figure 2.3a shows an artificially small resolution due to the small energy range (14.4 GeV - 20 GeV) in which the resolution is measured. Figure 2.4 shows the distributions of the asymmetry variable in the Monte Carlo simulation, where the effects of the low energy cut-off have less effect. Figure 2.5 summarizes these plots by showing $\frac{\sigma_{p_T}}{p_T}$ as a function of p_T^{event} for both the data and the Monte Carlo simulation. Both distributions in figure 2.5 are fitted with a function of the form:

$$\frac{\sigma_{p_T}}{p_T} = \sqrt{\frac{N^2}{p_T^2} + \frac{S^2}{p_T} + C^2} \tag{2.5}$$

in the range 30-120 GeV, shown by the solid lines. The values for the fitted parameters are shown in table 2.1 for both data and Monte Carlo simulation. The difference in resolution between data and the Monte Carlo simulation is demonstrated with the dotted curved line, which is the squared difference between the fitted data and the Monte Carlo simulation resolution functions. The Monte Carlo simulation underestimates the energy resolution of the jets. This can be attributed to a lack of non-linearity corrections of the energy measured in each calorimeter cell, as well as an incorrect modelling in the simulation of the noise in the calorimeter.

	N	S	C
Data	4.5 ± 1.7	1.3 ± 0.2	0.087 ± 0.034
MC	3.4 ± 0.72	0.91 ± 0.065	0 ± 0.10

Table 2.1: *Fit parameters used to fit the distributions in figure 2.5*

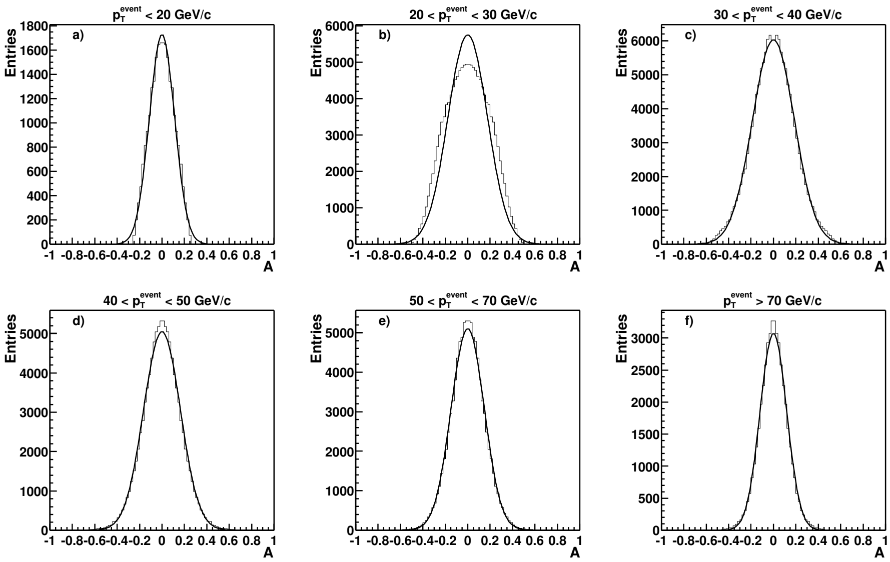

Figure 2.3: *Asymmetry distribution for data jets in different bins of* p_T^{event}.

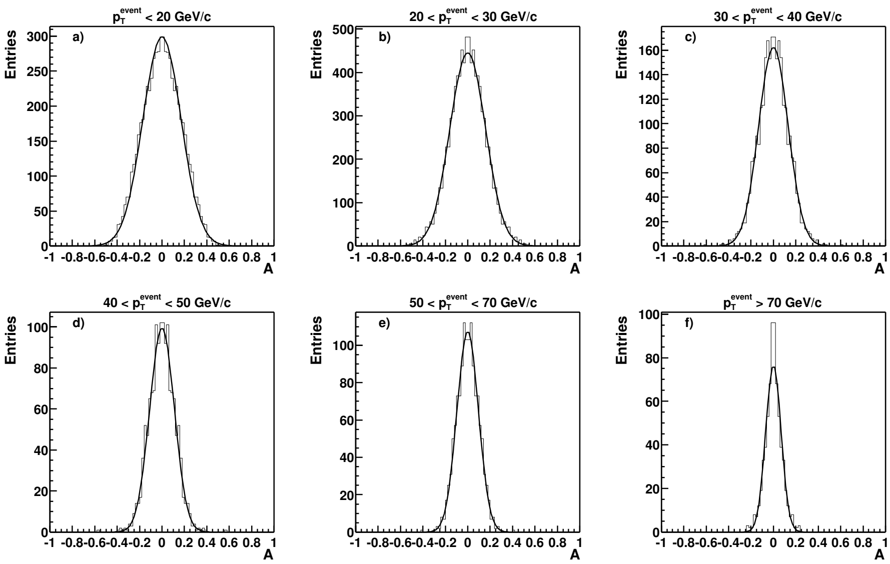

Figure 2.4: *Asymmetry distribution for jets in the Monte Carlo simulation, in different bins of* p_T^{event}.

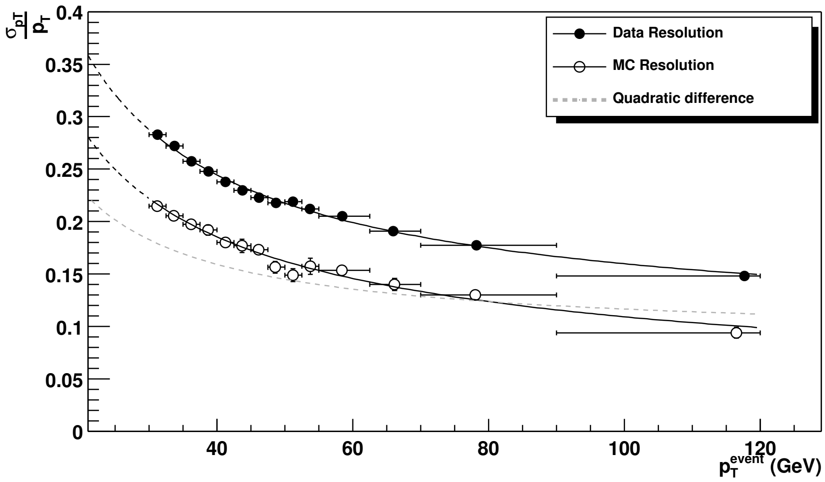

Figure 2.5: *Jet resolution as function of* p_T^{event}*, in the data (solid circles) and in the Monte Carlo simulation (open circles). The curved line represents the squared difference between data and the resolution in the Monte Carlo simulation.*

2.1.2 Jet Direction Resolution

The resolution with which the direction of the jet axis in η, ϕ is measured becomes important later in this analysis, when Monte Carlo templates are used to fit to the data. Especially the difference between the Monte Carlo and the data resolution is important. To get a handle on the resolution with which the jet axis direction is determined, samples of di-jet events are extracted from the data and the Monte Carlo simulation using the same selection criteria as in the previous section. From the di-jet events in these samples, the differences in η and ϕ are plotted in figure 2.6 for both data jets and Monte Carlo jets. The difference in η does not represent the resolution of the measurement of the η direction of the jets, since there is no need for an energy balance in η. The difference in ϕ does represent a resolution, since it is the deviation of one jet from the back-to-back axis in di-jet events. For the Monte Carlo templates deduced later, it is important that this resolution is similar in the data as in the Monte Carlo simulation, as is shown.

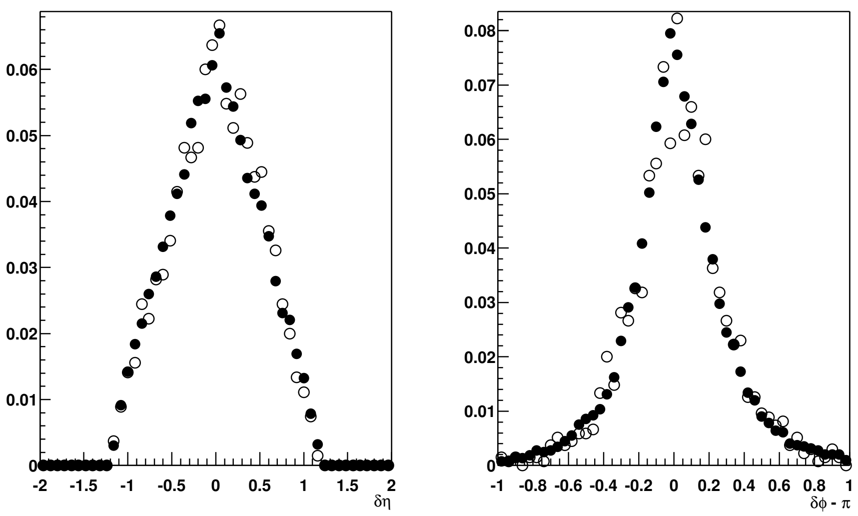

Figure 2.6: *Jet direction resolution in η and ϕ in data (solid circles) and the Monte Carlo simulation (open circles).*

2.2 Muon Reconstruction

2.2.1 Segment Reconstruction Efficiency

The segment reconstruction algorithm requires the presence of at least two wire hits to reconstruct a segment. The reconstruction efficiency for these segments is extracted from the data sample using central tracks that are extrapolated to the muon system. The A-layer segment reconstruction efficiency is calculated by extrapolating central tracks to the BC-layer and matching these tracks with present reconstructed BC-segments (see figure 2.2.1a). These BC-segments are required to consist of at least 3 wire hits in addition to a scintillator hit. The time measured with the scintillator hit is required to be within the trigger gate to reduce the contamination by cosmic rays in the sample. In addition, a scintillator hit in the A-layer that matches the extrapolated central track is required, and the event has to be triggered by the Level 1 muon trigger used (see section 1). These latter two requirements are needed to avoid the correlation of the muon reconstruction efficiency with the Level 1 muon trigger efficiency. In the Level 1 muon trigger, the presence of scintillator hits in the A- and B/C-layers is already required, and double counting of the scintillator hit efficiency has to be avoided. Reconstructed segments present in the A-layer, with at least 3 wire hits, are matched with this extrapolated track in the drift plane to calculate the reconstruction efficiency of A-layer segments. The efficiency found in this manner for A-layer segments is shown in figure 2.8 to be $92.7 \pm 0.9\%$ in the central region, and $91.5 \pm 0.6\%$ in the forward region, where the errors are statistical only.

A similar method is applied to find the reconstruction efficiency of BC-layer segments. Central tracks are propagated to the muon system, where they are matched with present A-layer segments and a scintillator hit in the B- or C-layer (see figure 2.2.1b). In the case of a match, the central tracks are matched with possible reconstructed BC-layer segments with at least 3 wire hits. This yields an efficiency of $90.6 \pm 2.7\%$ in the central region, and $97.5 \pm 1.2\%$ in the forward region, as illustrated in figure 2.9.

This algorithm is validated with a Monte Carlo sample by calculating the efficiency with the above procedure. Figure 2.8 shows the reconstruction efficiency for A-layer segments, figure 2.9 for BC-layer segments. The efficiencies found from the Monte Carlo simulation are compatible with the efficiencies found in the data, except for the central efficiency of the BC-layers. This can be attributed to an overestimation of the efficiency of the B- and C-layers in the simulation, and effects of the worse alignment in the data.

2.2.2 Local muon reconstruction efficiency

The reconstruction efficiency of the algorithm is measured by using extrapolated central tracks that have a matching A-layer and a matching BC-layer segment.

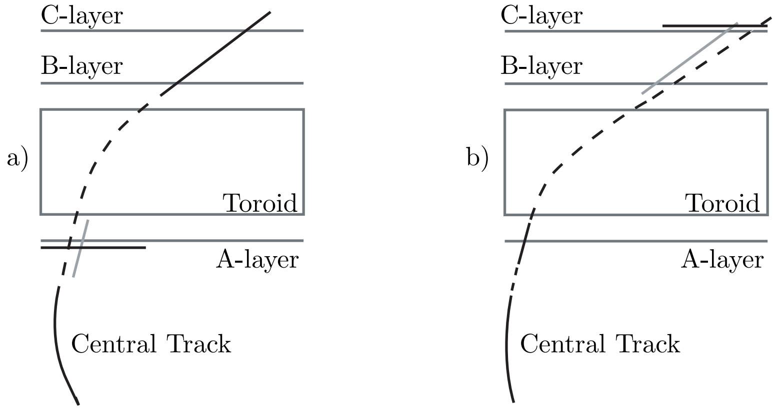

Figure 2.7: *Schematic overview for the calculation of the segment reconstruction efficiency. Figure a) shows the calculation of the A-layer segment reconstruction efficiency, using an extrapolated central track matched with a reconstructed BC-layer segment and an A-layer scintillator hit. Figure b) shows the calculation of the BC-layer segment reconstruction efficiency, using an extrapolated central track matched with a reconstructed A-layer segment and a C-layer scintillator hit.*

	Data	Monte Carlo
A-layer, central	$92.7 \pm 0.2\%$	$90.8 \pm 0.5\%$
A-layer, forward	$91.5 \pm 0.1\%$	$91.1 \pm 0.6\%$
BC-layer, central	$90.6 \pm 0.6\%$	$95.8 \pm 0.6\%$
BC-layer, forward	$97.5 \pm 0.1\%$	$98.5 \pm 0.3\%$

Table 2.2: *Segment reconstruction efficiencies. The efficiencies for Monte Carlo are calculated by applying the same algorithm on the Monte Carlo as on the data.*

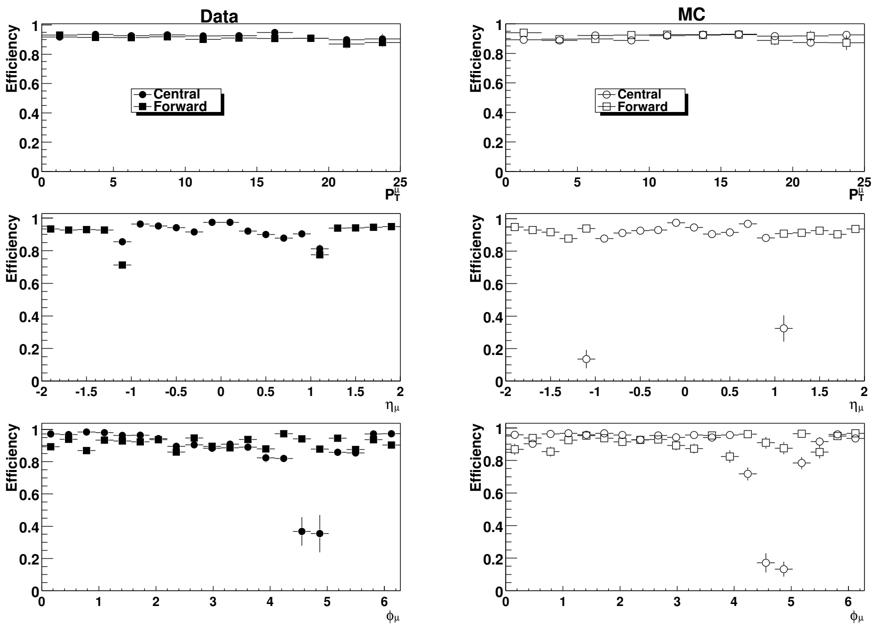

Figure 2.8: *A-layer efficiency as a function of p_T, η and ϕ for data on the left side, Monte Carlo on the right side. Central region efficiency displayed by black circles, forward region by open circles.*

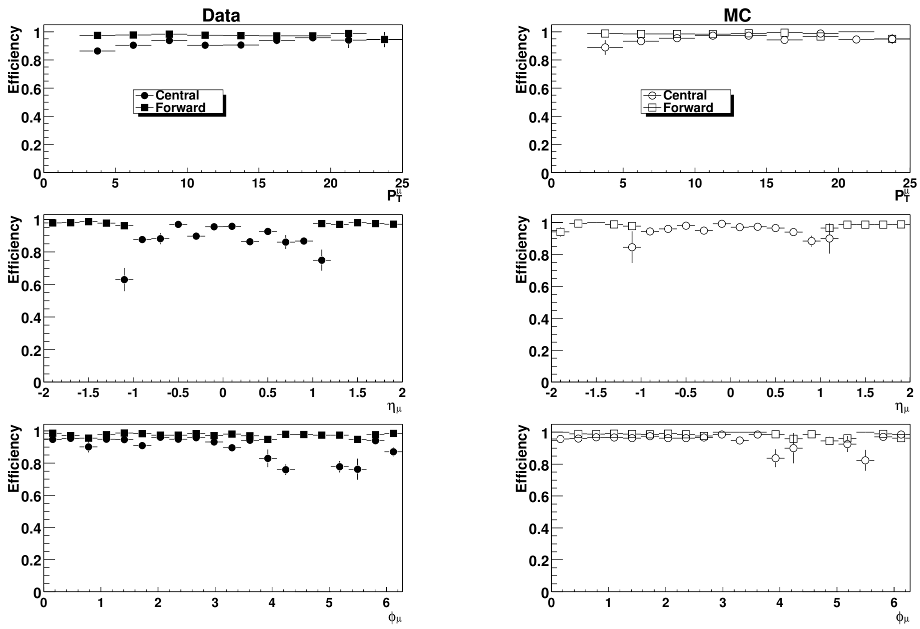

Figure 2.9: *BC-layer efficiency as a function of p_T, η and ϕ for data on the left side, Monte Carlo on the right side. Central region efficiency displayed by black circles, forward region by open circles.*

	Data	Monte Carlo
Fit efficiency central	$55.3 \pm 0.2\%$	$60.0 \pm 1.4\%$
Fit efficiency forward	$74.6 \pm 0.4\%$	$79.7 \pm 1.0\%$

Table 2.3: *Muon track fit efficiency. The efficiencies for Monte Carlo are calculated by applying the same algorithm on the Monte Carlo as on the data.*

The spatial matches used between the central track and the segments are the same as the ones used to calculate the respective segment reconstruction efficiencies. The local muon efficiency is now calculated by dividing the number of muon tracks that pass the quality and kinematic cuts, and originate from the segments matched to the central track, by the number of central tracks with matching segments. Figure 2.10 shows the efficiency of the track fitting algorithm in both the data and the Monte Carlo simulation; table 2.3 summarizes the results. The Monte Carlo simulations overestimates the fit efficiency, especially in the bottom octants ($3.8 < \phi < 5.3$). This can be attributed to the fact that the Monte Carlo simulation uses an ideal geometry, while the data is reconstructed with a less well aligned geometry.

To calculate the final muon reconstruction efficiency, the found fit efficiency has to be folded with the efficiency to find both an A-layer and a BC-layer segment. In addition, we also have to correct for the fact that we already required the presence of scintillator hits, which was done to avoid biases with the calculation of the trigger efficiency. This correction is calculated from the data by selecting events for which the muon trigger fired and a central track is present that matches with a muon track. This muon track is required to have at least 2 wire hits in the A-layer, at least 3 wire hits in the BC-layer and a converged fit. The scintillator correction is than calculated as:

$$\epsilon_{scintillator} = \frac{Number\ of\ muon\ tracks\ with\ matching\ scintillator\ hits}{Number\ of\ muon\ tracks} \tag{2.6}$$

This results in a correction of $94.1 \pm 0.4\%$ in the central region, and $99.5 \pm 0.1\%$ in the forward region. This correction is calculated in the Monte Carlo simulation in a similar fashion, except that the requirement that the trigger fired is dropped. This results in a correction of $88.6 \pm 1.1\%$ in the central region, and $92.0 \pm 1.0\%$ in the forward region.

Accounting for all these effects results in a reconstruction efficiency of $43.7 \pm 0.8\%$ and $66.2 \pm 0.3\%$ in the central and forward region respectively. In the Monte Carlo simulation these numbers are $46.2 \pm 0.2\%$ and $65.8 \pm 1.4\%$ (see figure 2.11 and table 2.4). To validate the algorithm with which these results are derived, regardless of the quality of the Monte Carlo simulation as compared with the data, the efficiency to find a reconstructed muon that passes the muon identification cuts is also extracted from the Monte Carlo truth information.

	Data	Monte Carlo	Monte Carlo Truth
Reconstruction efficiency central	$43.7 \pm 0.8\%$	$46.2 \pm 2.0\%$	$44.0 \pm 0.5\%$
Reconstruction efficiency forward	$66.2 \pm 0.3\%$	$65.8 \pm 1.4\%$	$62.1 \pm 0.7\%$

Table 2.4: *Muon track fit and final reconstruction efficiencies. The efficiencies for Monte Carlo are calculated by applying the same algorithm on the Monte Carlo as on the data; the efficiency in the Monte Carlo Truth table are calculated with the true Monte Carlo information.*

This is done by using a spacial match of $\delta R < 0.3$ between the Monte Carlo muon (at the vertex) and the reconstructed muon in the muon system. This results in an efficiency of $44.0 \pm 0.5\%$ in the central system, and $62.1 \pm 0.7\%$ in the forward system. The difference between the result of the algorithm applied on the Monte Carlo simulation and the result from the Monte Carlo truth, 2.2% and 3.7% is taken as the systematic error on the measurement of the muon track reconstruction efficiency.

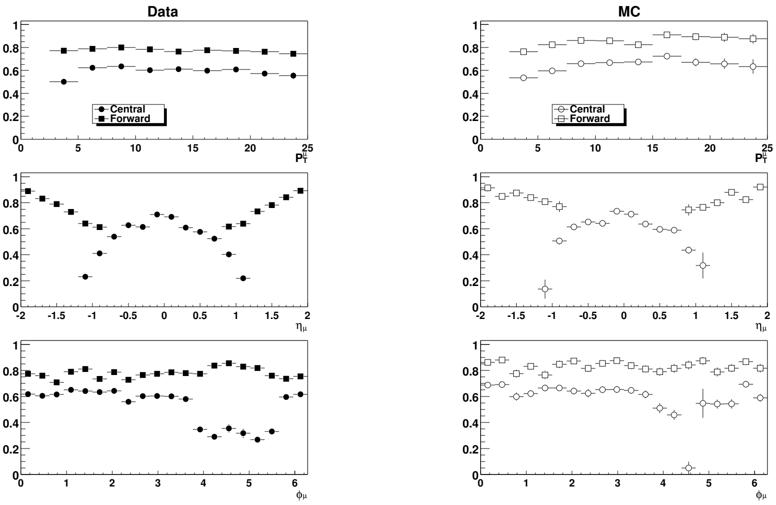

Figure 2.10: *Efficiency as a function of p_T, η and ϕ for fitting a muon track from two present segments*

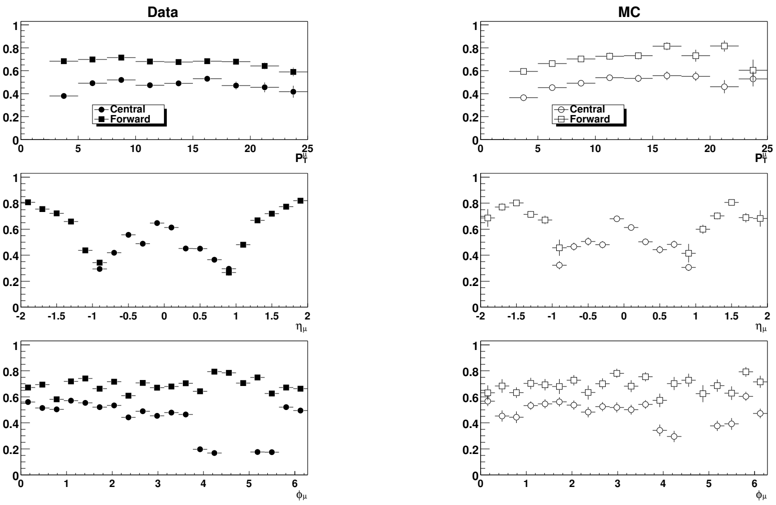

Figure 2.11: *Total muon reconstruction efficiency*

2.2.3 Local muon resolution

The resolution of the muon track momentum measurement is calculated by using central tracks. These tracks are propagated to the A-layer of the muon system, where they are matched with tight[1] muon tracks. Since the p_T resolution of central tracks is negligible at $\sim 5\%$ in the p_T range of muons in the sample (see figure **??**), the local muon track momentum resolution can be measured by comparing the local muon track momentum with that of the matched central track. Figure 2.12 shows the resolution Δ of the local muon track momentum for data, as well as for the Monte Carlo simulation, where

$$\Delta = p_T^C \left(\left(\frac{Q}{p_T} \right)^C - \left(\frac{Q}{p_T} \right)^L \right) \tag{2.7}$$

with the C superscript denoting central tracks and the L superscript denoting local muon tracks. The quadratic difference between the two distributions is displayed by the gray dotted line. The significantly worse resolution in data can be attributed to the larger hit residuals in the data. This causes a degradation of the segment resolution and hence a worse p_T resolution of the fitted local muon track. An additional effect is caused by the fact that the Monte Carlo simulation uses an ideal description of the muon detector. The detector description used to reconstruct the data is based on survey data with no further alignment, which can cause the position of the chambers in the assumed geometry to be different from the true geometry by a number of millimeters, further worsening the p_T resolution of the fitted muon track.

The direction resolution in η and ϕ of the muon tracks is also measured using central tracks. To estimate the η resolution of the muon tracks, central tracks are propagated to the A-layer, and matched with tight muons in p_T and ϕ. The ϕ resolution is measured in a similar fashion. These resolutions are shown in figure 2.13 for data and the Monte Carlo simulation. The η resolution of the Monte Carlo simulation is better than the η resolution in the data. This is again due to the underestimation of the p_T resolution in the Monte Carlo simulation. Smearing the p_T of the local muon tracks in the Monte Carlo simulation results in similar η resolutions in the simulation as in the data.

[1] See section 3.1

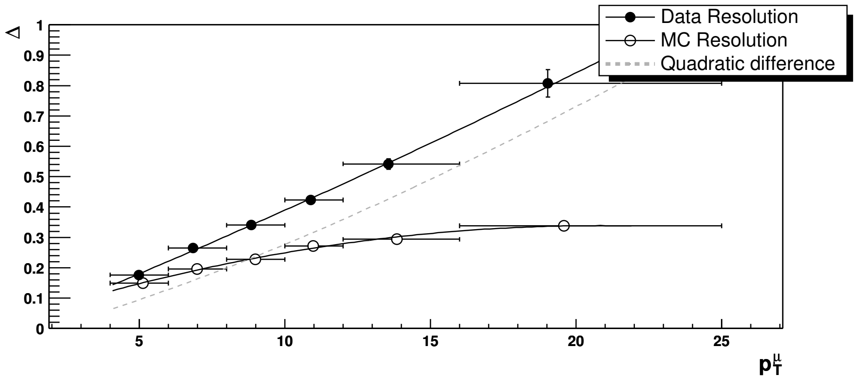

Figure 2.12: *Muon momentum resolution as function of P_T^μ*

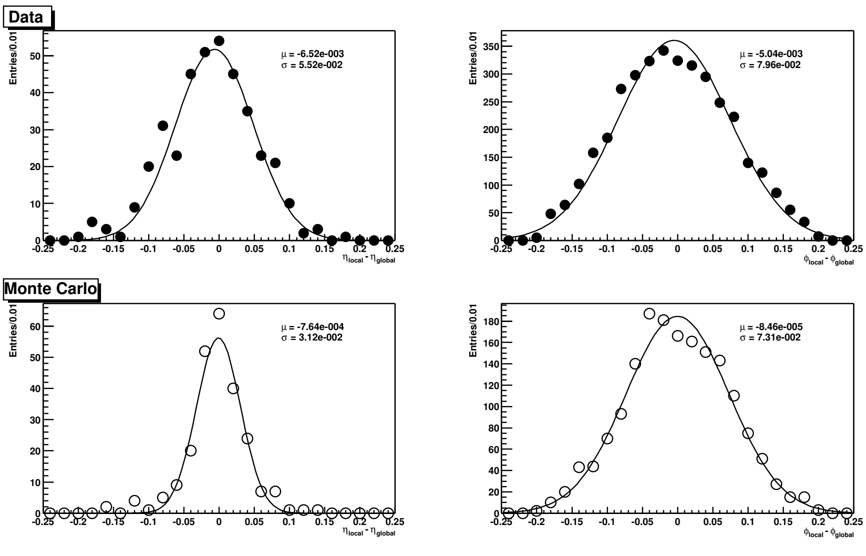

Figure 2.13: *Muon direction resolution in η and ϕ for data and Monte Carlo*

Chapter 3

Data Selection

This analysis uses data taken with the DØ detector in the period February 28^{th} until May 10^{th}. The sample is divided in 4 parts, according to the version of the trigger with which the data was taken. Events in the sample are further selected on trigger, physics and quality criteria, namely:

- A $mu1ptxatxx\_CJT5$ Level 1 trigger requirement, see section 1;
- The presence of a reconstructed muon and a reconstructed jet, with the additional constraint that $\delta R(jet, \mu) < 0.7$;
- The run is qualified as good in the run quality database.

Table 3.1 lists the resulting data sample, containing 361037 events and corresponding to a total integrated luminosity of 3.4 pb^{-1}.

3.1 Muon Identification

Due to the low reconstruction efficiency of tracks in the central tracking system during most of the data taking period, the muon reconstruction and identification can make no use of these tracks, but has to rely solely on the information

Trigger	Number of events	Integrated luminosity (nb^{-1})
global_CalMuon4.20	92900	862.7
global_CalMuon5.00	33201	331.1
global_CalMuon5.01	209190	2003
global_CalMuon5.10	25746	246.0
Total	361037	3442.8

Table 3.1: *Data sample used in the analysis*

of the muon system. To still get a reasonable momentum and direction measurement of the muon, it is required to pass all three layers and hit a minimum number of detector components in those layers:

- At least 2 wire hits in the A-layer;
- At least 1 matching scintillator hit in the A-layer;
- At least 3 wire hits in the combined B and C-layer;
- At least 1 matching scintillator hit in the B or C-layer.

In addition, the χ^2 of the fit of the A and B/C layer segments is required to be greater than zero, which indicates a converged track fit. Furthermore, kinematic cuts are applied to the muon:

- $p_T^\mu > 4$ GeV/c, to be well above the implicit cut of 3 GeV/c that a muon requires to penetrate the toroid;
- $|\eta_\mu| < 0.8$, to avoid the overlap regions between the forward and central system at $|\eta| \approx 1$.

The properties of the reconstructed muons after these selections is shown in figure 3.1. Even though the η distribution is symmetric around $\eta = 0$, as expected, it is not flat. This is partly due to the L1 trigger efficiency, which has an η dependance (see figure 1.3), but also due to the reconstruction efficiency, which is not flat in η. The ϕ distribution clearly shows the hole in the detector at $\frac{5\pi}{4} < \phi < \frac{7\pi}{4}$, as well as the octant boundaries at $\phi = \frac{\pi}{4}$ and $\phi = \frac{3\pi}{4}$, where the muon wire chambers change orientation (the effect of the octant boundaries at $\phi = \frac{5\pi}{4}$ and $\phi = \frac{7\pi}{4}$ are also present but obscured by the larger effect of the hole in the bottom).

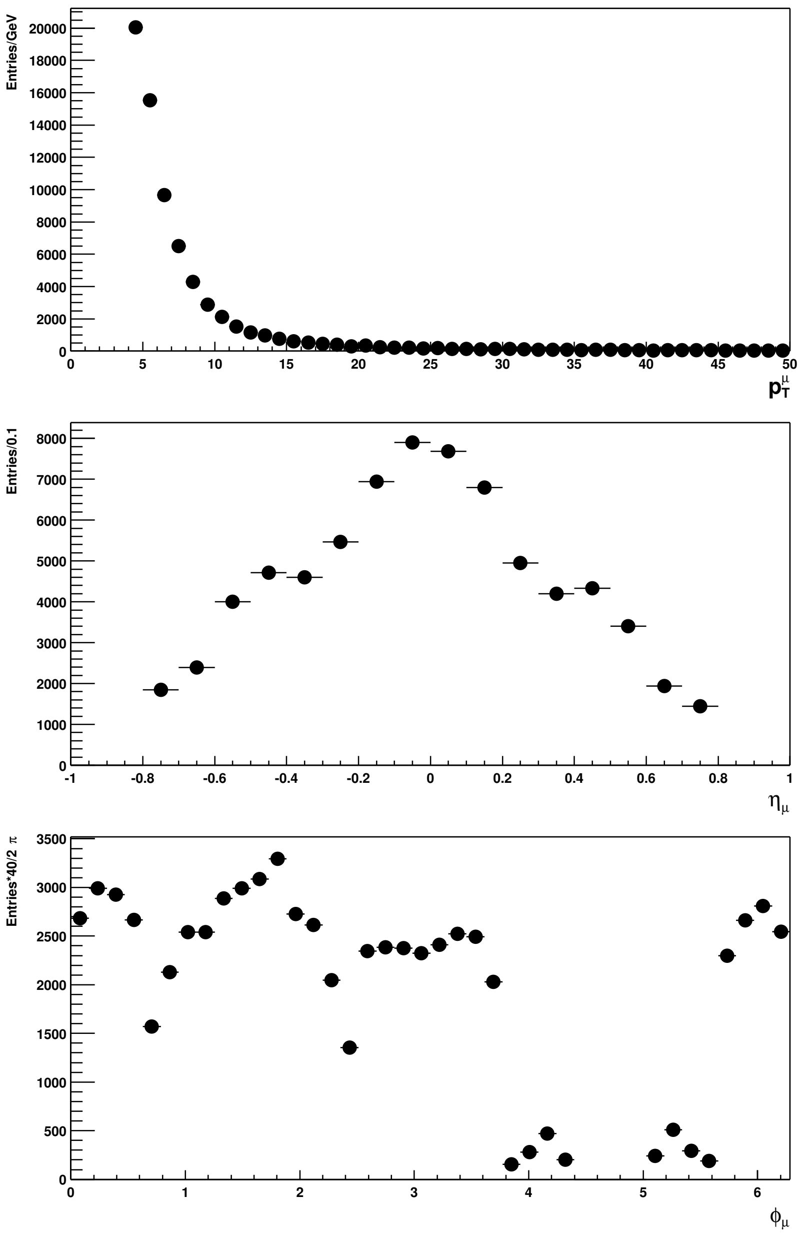

Figure 3.1: *p_T, η and ϕ of reconstructed muons, after applying kinematic cuts. Error bars are drawn but not visible.*

3.2 Jet Selection and Identification

The major background to physics jets are hot cells, which are not created by an energy deposition of a particle passing through the cell. Even though these are partly removed by the hot cell suppression, some still remain and are reconstructed into fake jets. To suppress these jets, the following cuts are applied (see figure 3.2):

- Hot Fraction < 10: the fraction between the hottest cell and the next to hottest cell should be lower than 10. A higher ratio points to an unbalanced jet in which the highest energy cell is probably a hot cell;
- $1 < n90 < 30$: n90 is the number of calorimeter towers that contain 90% of the jet's energy. If this number is 1, this again points to an unbalanced jet consisting of one tower. If it is greater than 30, the jet consists of a high number of towers which each contain little energy. These are mainly jets consisting fully of noisy cells.
- Coarse Hadronic Fraction (CHF) < 0.4: The energy fraction of the total energy of the jet that it deposits in the last layer of the calorimeter;
- Electromagnetic Fraction between 0.05 and 0.95: electrons deposit more than 95% of their energy in the electromagnetic calorimeter. The lower bound is used to cut away hot cells in the hadronic calorimeter;

In addition, kinematic cuts are placed on the jets:

- $|\eta| < 0.6$, to avoid the effects of the jets overlapping with the Inter Cryostat region;
- $E_T^{corr} > 20$, to be well above the 14.4 GeV cut in the jet reconstruction.

with E_T^{corr} the transverse energy of the jet, corrected by applying the Jet Energy Scale correction. The resulting E_T, η and ϕ distributions of the reconstructed jets are plotted in figure 3.3. The ϕ distribution shows an 8-fold structure, due to the requirement of an associated muon with $\delta R(jet, \mu) < 0.7$. Less muons are reconstructed in the region $\frac{5\pi}{4} < \phi < \frac{7\pi}{4}$, resulting in less associated proper jets in that region. Also, other side jets in the region $\frac{\pi}{4} < \phi < \frac{3\pi}{4}$ are suppressed by this effect.

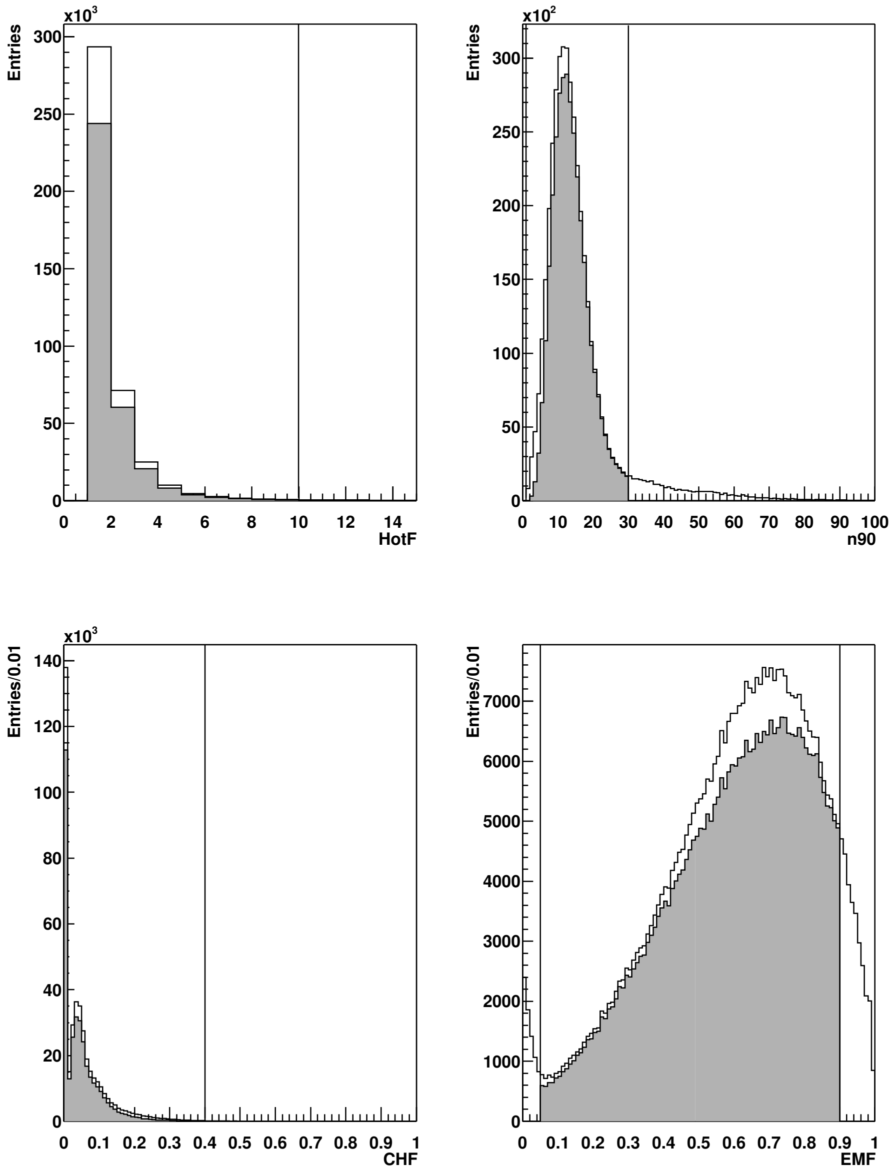

Figure 3.2: *Properties of jets used to suppress fake jets, before (open histograms) and after (solid gray histograms) ID cuts.*

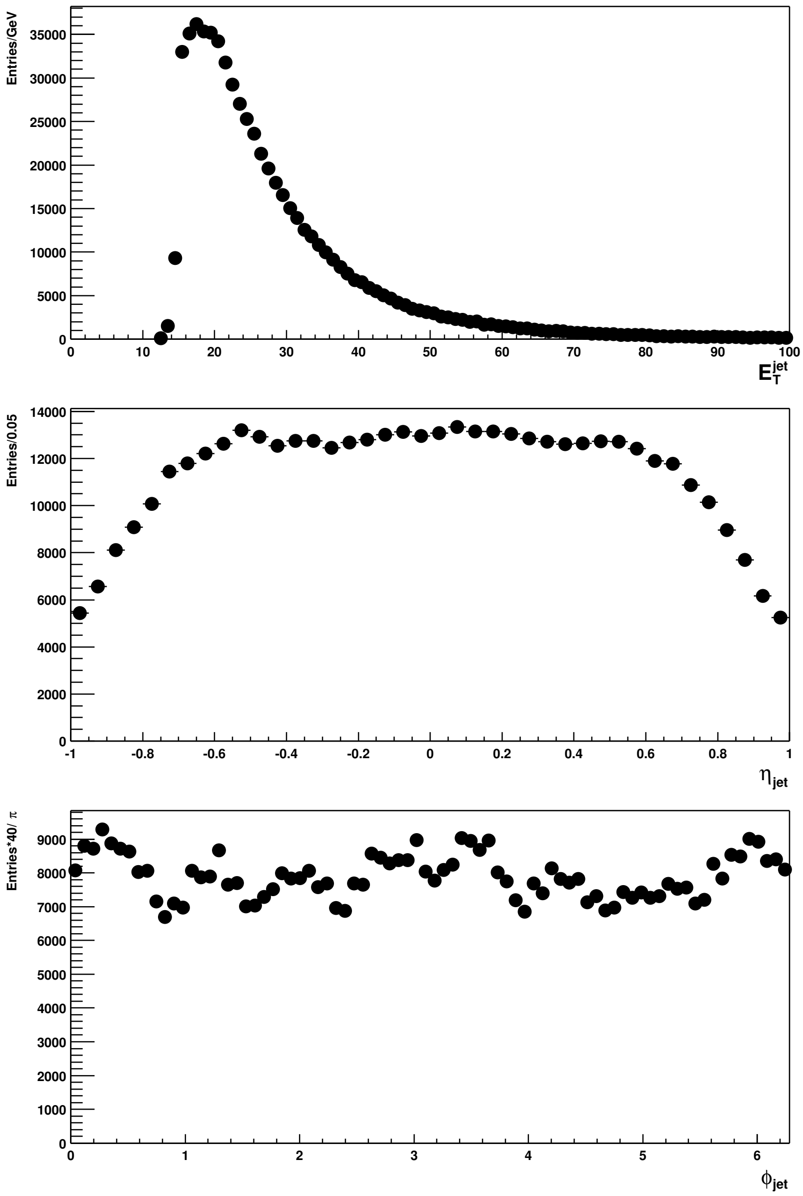

Figure 3.3: *E_T, η and ϕ distribution of reconstructed jets, after selection and kinematic cuts.*

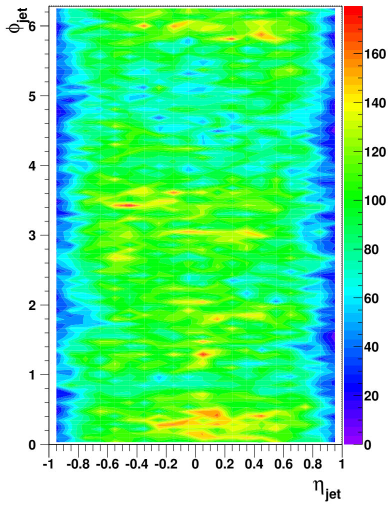

Figure 3.4: ϕ_{jet} *versus* η_{jet}.

3.2.1 Jet ID Efficiency

Not only do the jet ID cuts as explained in the previous section cut away the fake jets, they also cut away a number of good jets for which a correction needs to be applied. The extent of this correction is calculated using di-jet events, in which one of the jets passes the ID criteria, and furthermore:

- Both jets have $|\eta| < 0.6$ and $E_T > 20GeV$, to be in the same fiducial volume as the jets in the data sample;
- The jets are back-to-back: $\Delta\phi < 175°$, and $\not{E}_T < 0.7p_T^{leading\ jet}$, to ensure a proper di-jet event;
- $E_{tot} < 2$ TeV, to remove events with noisy calorimeter readout.

The ID efficiency can be extracted from this sample using the following definition:

$$\epsilon_{ID} = \frac{Number\ of\ other\ side\ jets\ passing\ ID\ cuts}{Total\ number\ of\ other\ side\ jets} \tag{3.1}$$

This efficiency is shown as a function of jet E_T, η and ϕ in figure 3.5, and averages to $94.2 \pm 0.1\%$. The ID efficiency as a function of jet E_T shows a turn-on curve for jets below 40 GeV. This turn-on curve is caused by the cut on the electromagnetic fraction of the jet - low energy jets deposit a higher fraction of their energy in the first layers of the calorimeter. This is demonstrated in figure 3.5 by the small crosses, which represent the jet ID efficiency without the EMF cuts. Without these cuts, the ID efficiency averages to $98.7 \pm 0.1\%$.

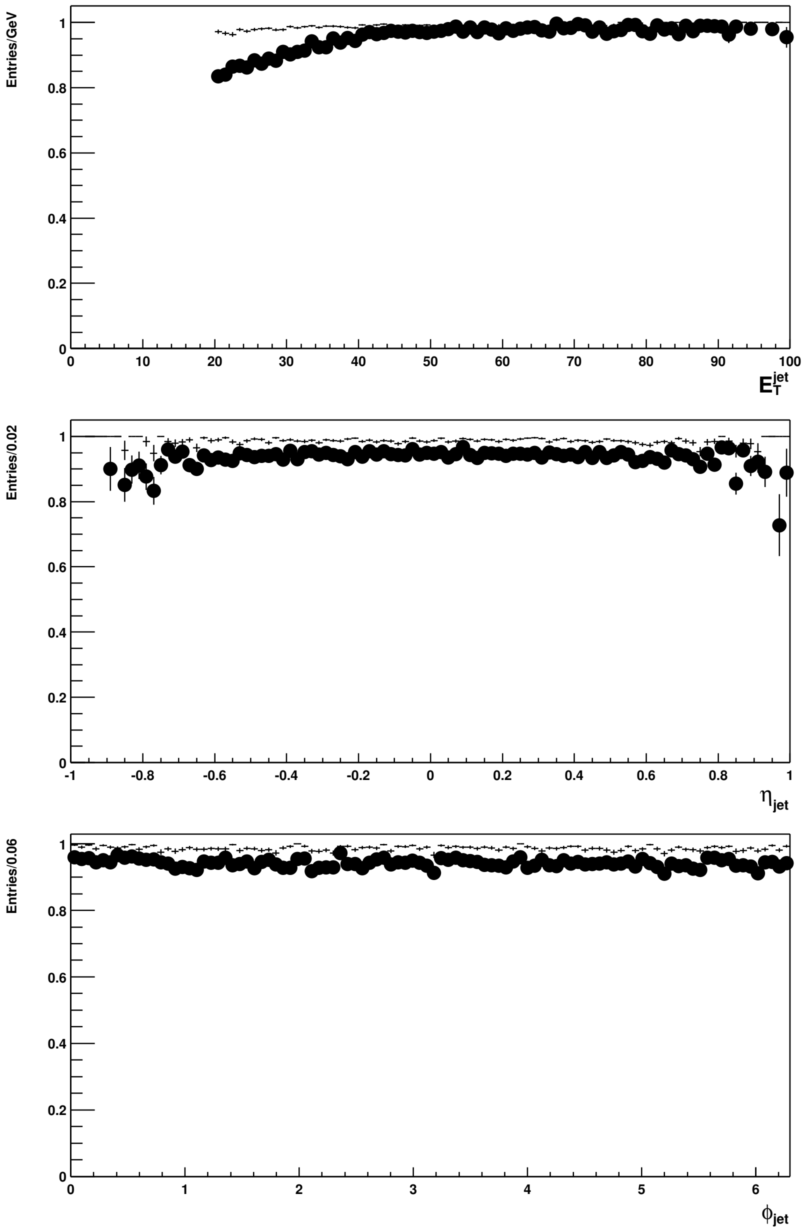

Figure 3.5: *Jet ID efficiency as function of E_T, η and ϕ. Black dots represent the efficiency after all cuts, the crosses represent the efficiency without the EMF cuts.*

Chapter 4

Muon + Jet Cross section

The first step towards the measurement of the b-jet cross section, with the b-jets tagged with a muon, is to measure the total $\mu + jet$ cross section as a function of jet E_T, $d\sigma/dE_T^{jet}$. Using the trigger and reconstruction efficiencies for jets and muons as derived in previous chapters, we will now measure $d\sigma/dE_T^{jet}$ in the Run II data set.

4.1 Differential cross section for muon + jet events

The sample used corresponds to a total of 3.4 pb^{-1} of integrated luminosity. To measure the differential cross section, each event needs to be scaled with the detection efficiency for that event and the total integrated luminosity:

$$\frac{d\sigma}{dE_T^{jet}} = \frac{1}{\epsilon(\mu, jet) \int \mathcal{L} dt} \frac{dN}{dE_T^{jet}} \tag{4.1}$$

Here, dN/dE_T^{jet} is the number of events in each E_T^{jet} bin, and $\epsilon(\mu, jet)$ is the weighted average efficiency of all trigger, reconstruction and identification efficiencies for the muons and jets in that E_T^{jet} bin. Figure 4.1 shows the μ + jet cross section as a function of E_T^{jet}, uncorrected for trigger, reconstruction and identification efficiencies, normalized to the appropriate integrated luminosity. In the next section, we will correct this cross section for these inefficiencies.

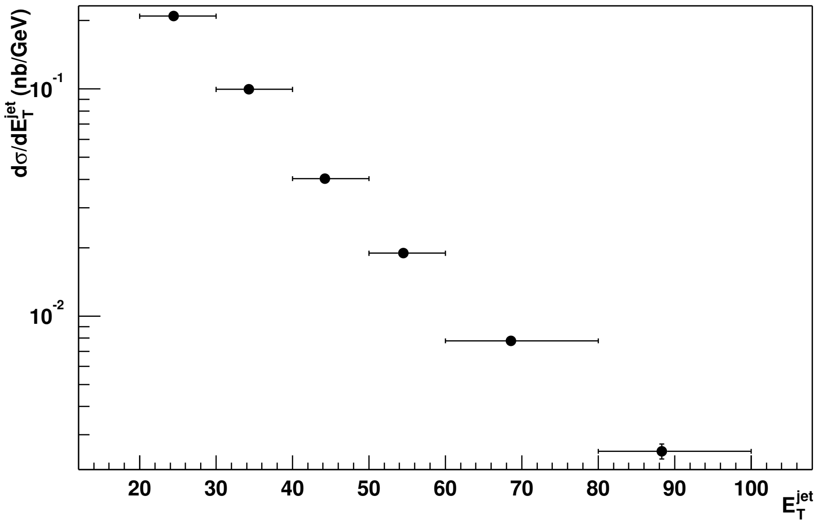

Figure 4.1: *$\mu + jet$ differential cross section, uncorrected for trigger, reconstruction and identification efficiencies. Statistical errors are shown only.*

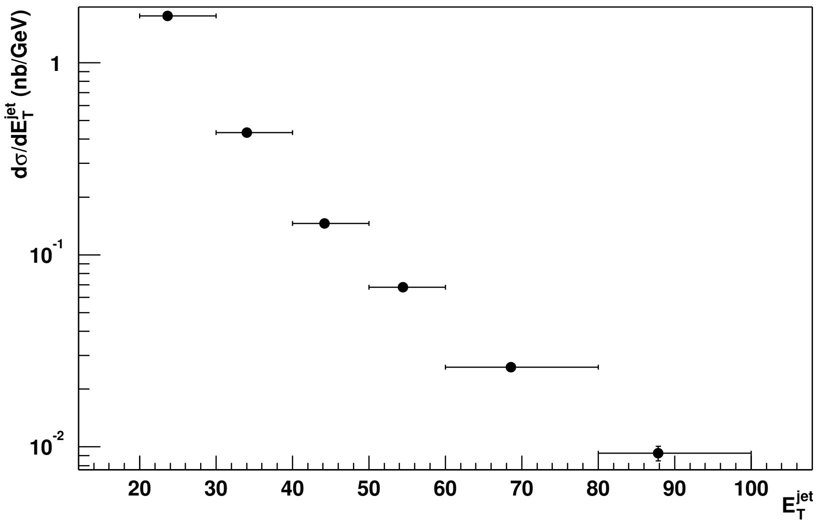

Figure 4.2: *$\mu + jet$ differential cross section, corrected for trigger, reconstruction and identification efficiencies. Statistical errors are shown only.*

4.1.1 Efficiency corrections

The correction of the measured cross section for the inefficiencies mentioned above is done on a jet by jet basis. For every jet, with associated muon, the possible dependence of the efficiency on the η, ϕ or p_T of the muon and jet is taken into account, and the weight with which the event enters in the cross section is updated accordingly. The effect that the error on each efficiency has on the cross section is determined by adding (subtracting) the error on each efficiency separately, and recalculating the cross section with this new efficiency. The difference this gives on the original cross section is taken as the error on the cross section, resulting from that source.

Level 1 calorimeter trigger

The μ+jet cross section is corrected for the Level 1 calorimeter trigger efficiency according to the turn-on curve shown in figure 1.1. The dominant systematic error on the trigger efficiency is due to the uncertainty of the Jet Energy Scale correction. This systematic error will be discussed in a later section. The effect of the remaining statistical error on the final cross section is shown by the open circles in figure 4.3.

Level 1 muon trigger efficiency

The level 1 muon trigger efficiency shows a dependence on both p_T and η (see figure 1.2). Due to statistical limitations, it is not possible to perform a full 2-dimensional calculation of the efficiency in (p_T, η) bins. Therefore, we first calculate the efficiency averaged over p_T but taking into account the η dependance. Then, the efficiency is calculated using an averaged η efficiency and taking into account the p_T dependence. The difference resulting from using these two different cross sections is taken as an additional systematic error on the Level 1 muon trigger efficiency. The effect of the resulting total error on the cross section is shown by the squares in figure 4.3.

Muon reconstruction efficiency

The muon reconstruction depends on p_T, η, and to a lesser extent, on ϕ. Since the physics is invariant in ϕ, we correct for the bottom in the detector by an overall scale factor. The dependence on p_T and η is taken into account in a similar fashion as done for the Level 1 muon trigger efficiency. The black circles in figure 4.3 show the systematic error on the cross section resulting from the errors on the muon reconstruction efficiency.

Jet Energy Scale correction

The Jet Energy Scale correction is already taken into account in the cross section as shown in figure 4.2. The uncertainty on the correction, of approximately 7%, is not. Again, the change on the measured cross section resulting from floating this error around the nominal Jet Energy Scale correction is taken as the systematic error. This is illustrated by the stars in figure 4.4.

The resulting μ+jet cross section, now with statistical and systematic errors is shown in figure 4.5.

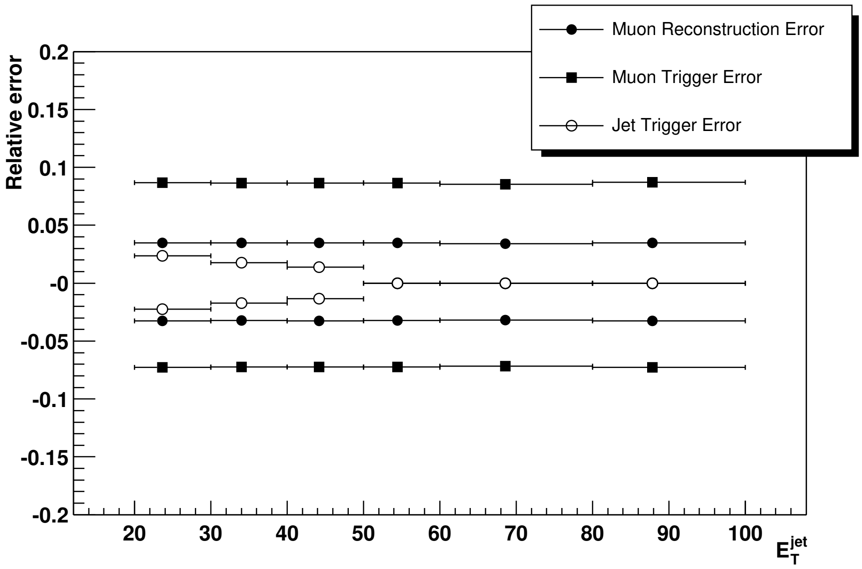

Figure 4.3: *Systematic errors on the $\mu + jet$ differential cross section, resulting from the trigger, reconstruction and identification efficiencies*

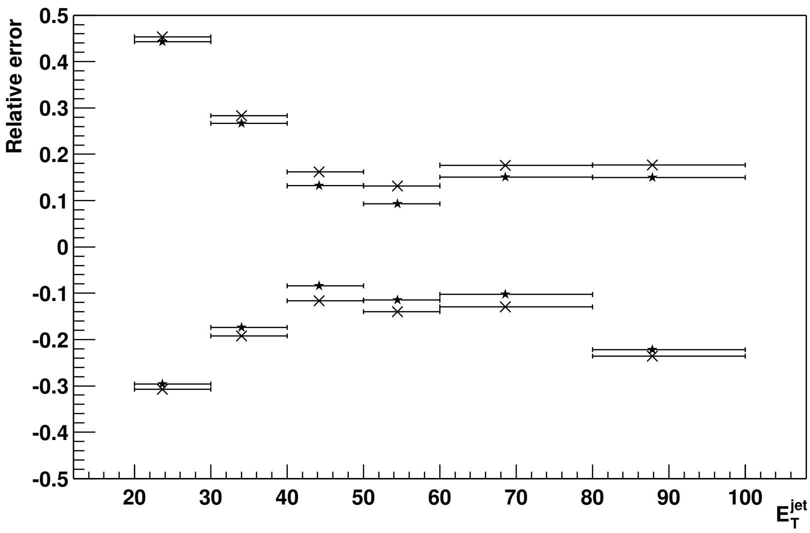

Figure 4.4: *Systematic error on the $\mu + jet$ differential cross section resulting from the uncertainty on the Jet Energy Scale (stars) and the total systematic error (crosses).*

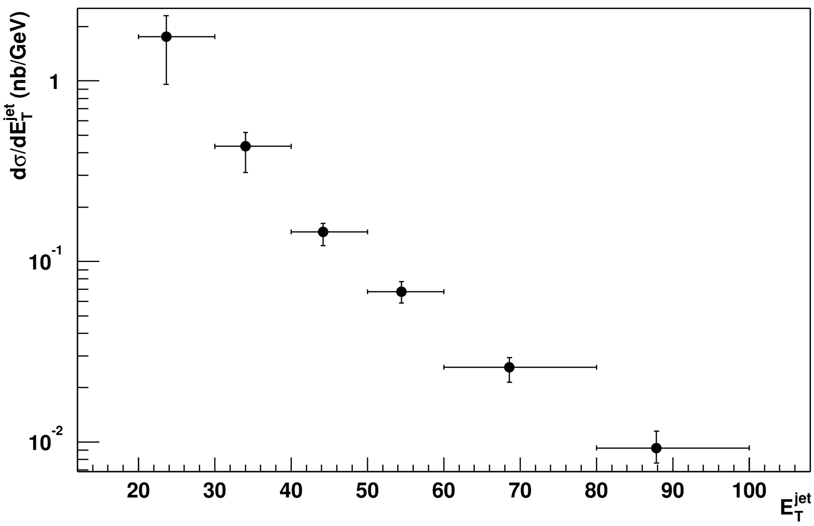

Figure 4.5: *μ+jet differential cross section, corrected for trigger, reconstruction and identification efficiencies. Full statistical and systematic errors shown.*

Chapter 5

B-jet cross section

We now proceed to extract the b-jet content from the μ+jet cross section we have measured in the previous chapter. This b-jet content results in a b-jet cross section measurement which needs unsmearing and acceptance corrections to result in a detector-independent b-jet cross section measurement.

5.1 Extracting the b-jet component

To extract the b-jet component from the $\mu + jet$ sample we use the properties of the muon with respect to the jet to identify direct $b \to \mu$ decays. The indirect decay, $b \to c \to \mu$ is considered a background. Other μ in jet producing processes which are a background are direct $c \to \mu$ decays, $\pi/K \to \mu$ decays and τ decays. At a higher p_T^μ, $W/Z \to \mu$ also starts to contribute. To select the b-jet component of the differential cross section, we use the P_T^{Rel} tagging variable, explained below.

5.1.1 P_T^{Rel} Tagging Variable

The P_T^{Rel} tagging variable is the transverse momentum of the muon with respect to the combined axis of the muon and jet (see figure 5.1). This variable is based on the decay of the quark in the jet: in the rest system of the meson or hadron that contains the b-quark, the muon gets a significant boost due to the mass difference of the b-quark and its decay products. This boost is lower when a c- or light quark decays. If the whole system is boosted along the quark momentum axis, the P_T^{Rel} variable is a measurement for the transverse boost of the muon with respect to the quark momentum axis. Figure 5.2 shows the P_T^{Rel} distribution measured in the data, with the following cuts:

- $E_T^{jet} > 20$ GeV;
- $|\eta^{jet} < 0.6$;
- $p_T^\mu > 6$ GeV/c;

- $|\eta^{\mu}| < 0.8$;
- $\delta R(jet, \mu) < 0.7$.

Figure 5.3 shows the P_T^{Rel} distribution extracted from the Monte Carlo simulation, for $b \rightarrow \mu$ decays, and background decays. The background decay template is extracted from approximately 1.5 million QCD events. Due to the low occurrence of high p_T muons in this sample, few events remain in the background template.

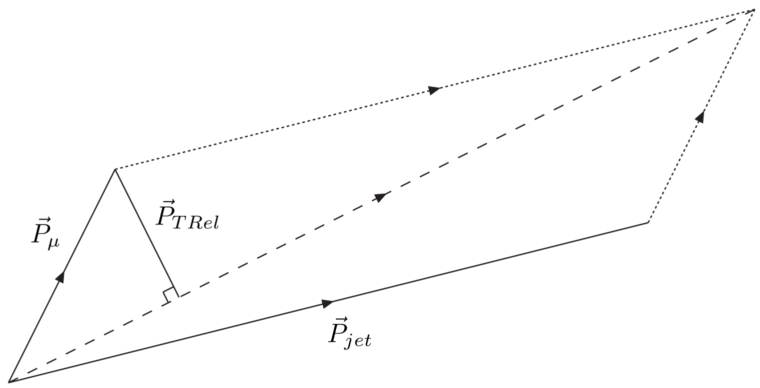

Figure 5.1: P_T^{Rel} definition

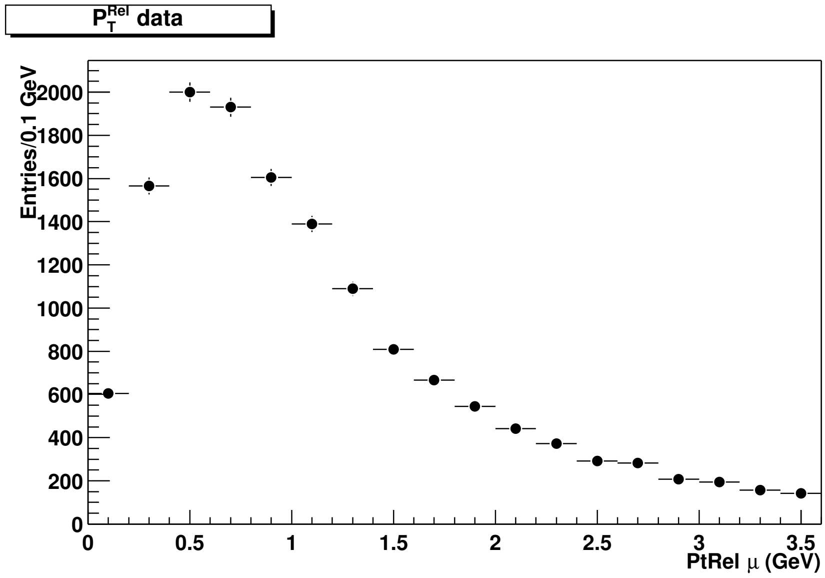

Figure 5.2: *Distribution of the P_T^{Rel} variable in the data sample.*

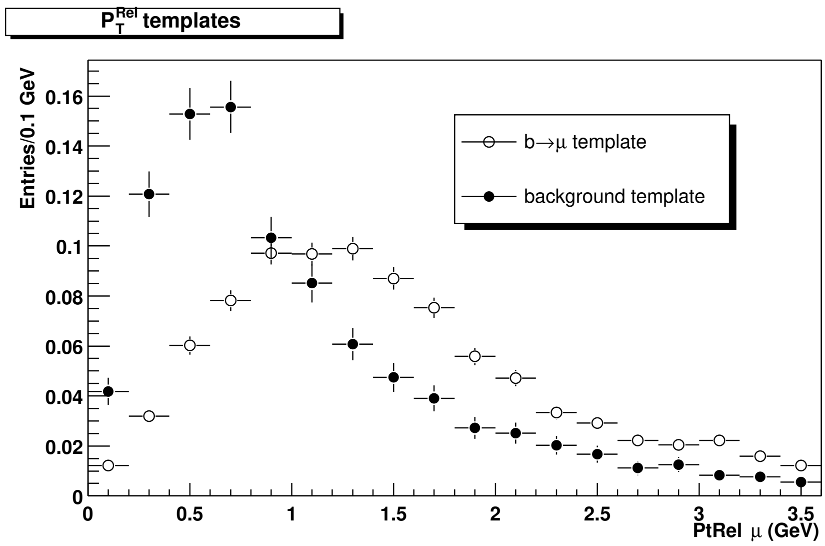

Figure 5.3: P_T^{Rel} *templates for signal and background, extracted from the Monte Carlo simulation.*

E_T^{jet} range	b-content	background content
20 - 25 GeV	0.39 ± 0.064	0.61 ± 0.073
25 - 35 GeV	0.22 ± 0.066	0.78 ± 0.077
35 - 50 GeV	0.24 ± 0.055	0.76 ± 0.068
50 - 100 GeV	0.14 ± 0.08	0.86 ± 0.10

Table 5.1: *Fit parameters used to fit the distributions in figure 5.6*

5.1.2 Template fit

We measure the b-jet content in bins of E_T^{jet}, where the number of bins is constrained by the statistical limitations of the background template. The following bins are chosen:

- 20 - 25 GeV;
- 25 - 35 GeV;
- 35 - 50 GeV;
- 50 - 100 GeV;

In each of these bins a fit is made of the templates to the data, according to:

$$\left(\frac{dN}{dE_T^{jet}}\right)_i^{data} = C_{b\to\mu}\left(\frac{dN}{dE_T^{jet}}\right)_i^{b\to\mu} + C_{non-b\to\mu}\left(\frac{dN}{dE_T^{jet}}\right)_i^{non-b\to\mu} \tag{5.1}$$

The fit is done using the HMCMLL fit, to take into account the statistics of the Monte Carlo templates. Figure 5.4 shows the result of the fit in the 20 - 25 GeV E_T^{jet} bin, with the Monte Carlo templates scaled with the results of the fit. Figure 5.5 shows the sum of the scaled templates together with the data distribution, showing a good saturation of the templates to the data. Table 5.1 summarizes the results of the fit in different bins. Figure 5.6 illustrates these numbers, together with a fit of the form:

$$a + \frac{b}{E_T^{jet}} \tag{5.2}$$

where $a = 0.13 \pm 0.064$ and $b = 125 \pm 58$.

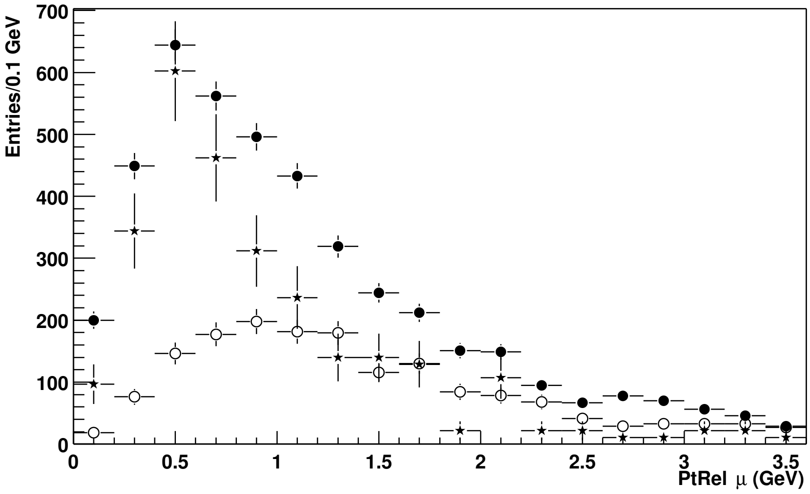

Figure 5.4: *Results of the fit in the jet energy range 20 - 25 GeV, with scaled templates.*

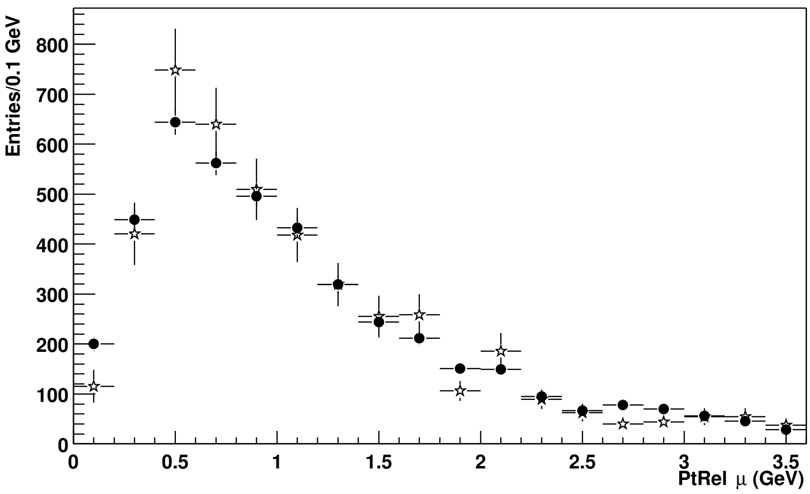

Figure 5.5: *Total fit of the templates to the data in the jet energy range 20 - 25 GeV.*

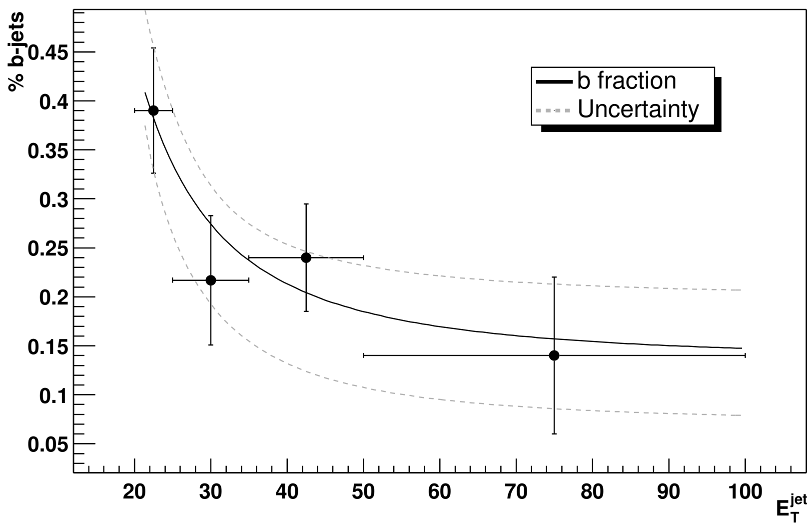

Figure 5.6: *B-jet content in the* μ*+jet sample as a function of* E_T^{jet}.

5.1.3 B-jet cross section

Using the b-jet content measured above, we can now measure the b-jet cross section by folding the μ+jet spectrum with the b-jet content. This is done on a bin-by-bin basis, where every bin is weighted with the b-jet content that corresponds to its E_T. The errors on the fit parameters of equation 5.2 are taken into account by propagating the full covariance matrix. This results in the b-jet cross section of figure 5.7, measured as a function of E_T^{jet}, as it is measured in the calorimeter. The next step will therefore be to correct for the detector effects on the measurement of the b-jet cross section.

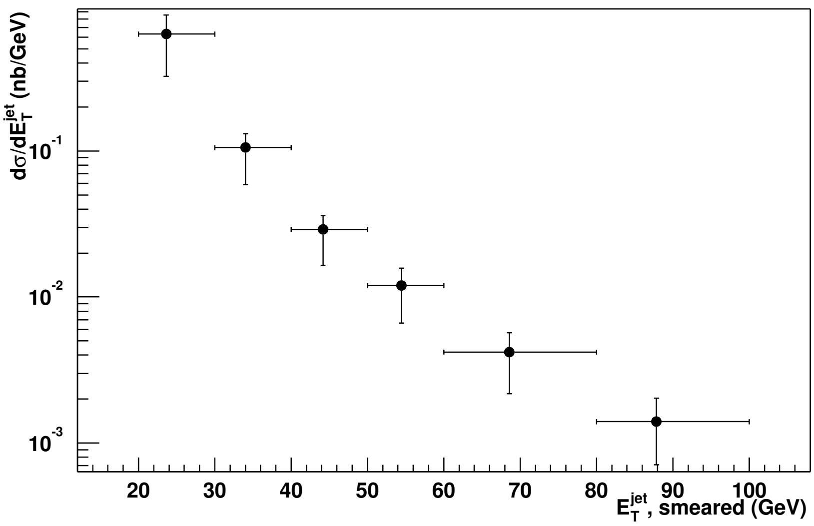

Figure 5.7: *B-jet cross section, with $B \to \mu$, as a function of calorimeter E_T^{jet}.*

5.2 Unfolding the b-jet cross section

The calorimeter measures the jet energy with a finite resolution, which distorts the shape of the measured cross section. To eliminate the effects of this distortion, we need to unfold the cross section with the resolution with which the calorimeter measures the jet energy (see section2.1.1). To this avail, we need to create an E_T dependent correction that reshapes the observed cross section in its true form, with resolution effects removed.

We start with an ansatz function with 3 free parameters, of the form:

$$F(E_T, \alpha, \beta, \gamma) = \alpha E_T^{\beta} \left(1 - \left(\frac{2}{\sqrt{s}} \right) E_T \right)^{\gamma} \tag{5.3}$$

where E_T is the true energy of the jet, α, β and γ are the free parameters, and $\sqrt{s}$ is the center of mass energy. This distribution is smeared with the E_T resolution, and fitted to the observed data distribution. After convergence of the fit, the parameters of the fit are substituted in the ansatz function, which then represents the unfolded cross section. The errors on the parameters of the jet energy resolution are analytically propagated to the resolution function using the full covariance matrix, and the error on the unfolded cross section resulting from this uncertainty is estimated by floating the resolution function within the errors. Figure 5.8 shows the result of this unfolding procedure. The dotted line is the ansatz function, with the fitted parameters inserted in the function. The solid line represents the smeared ansatz function, and is compared with the b-jet cross section. Figure 5.9 shows the ratio of the smeared ansatz function with the ansatz function, with the error bars coming from the uncertainty on the jet energy resolution. The smeared b-jet cross section is now scaled with this ratio, taking into account its errors. This results in the unsmeared b-jet cross section as shown in figure 5.10.

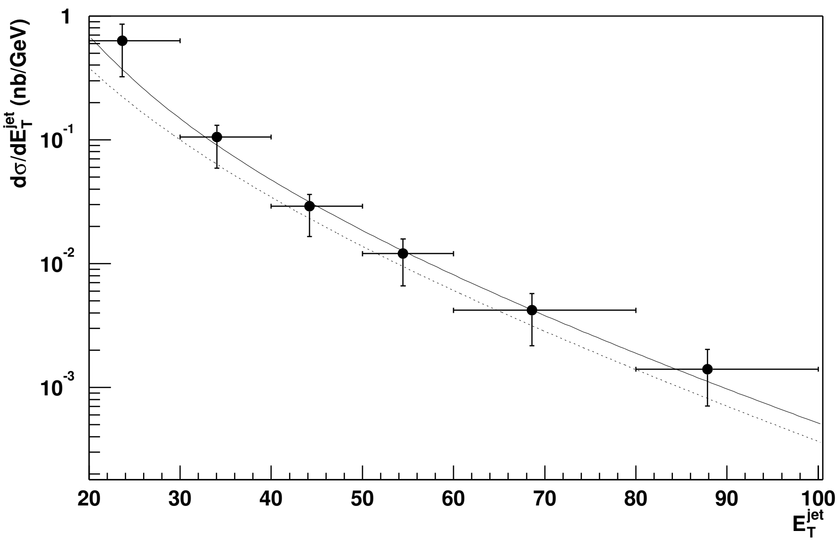

Figure 5.8: *Result of the unfolding procedure on the b-jet cross section. The dotted line represents the final ansatz function, with the solid line representing the smeared ansatz function. The smeared b-jet cross section is represented by the dots.*

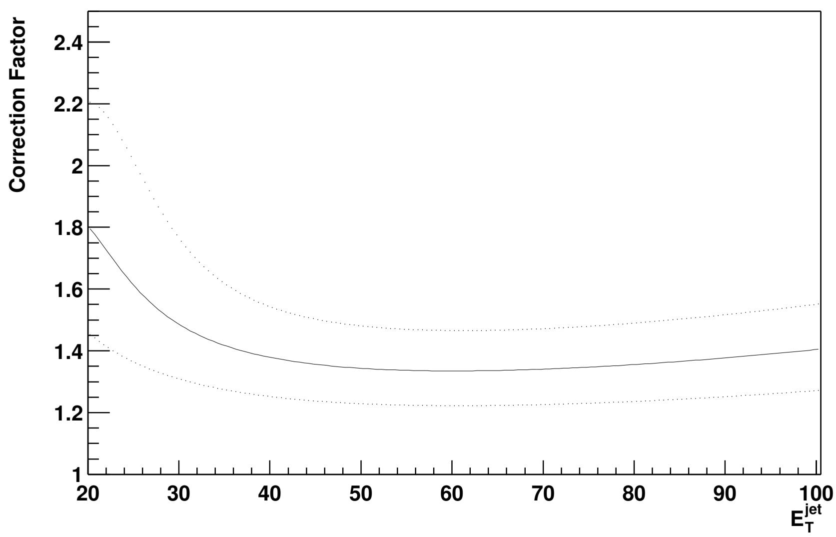

Figure 5.9: *The ratio between the smeared ansatz function and the ansatz function. The dotted lines represent the errors on the ratio that are coming from the uncertainty on the jet energy resolution function.*

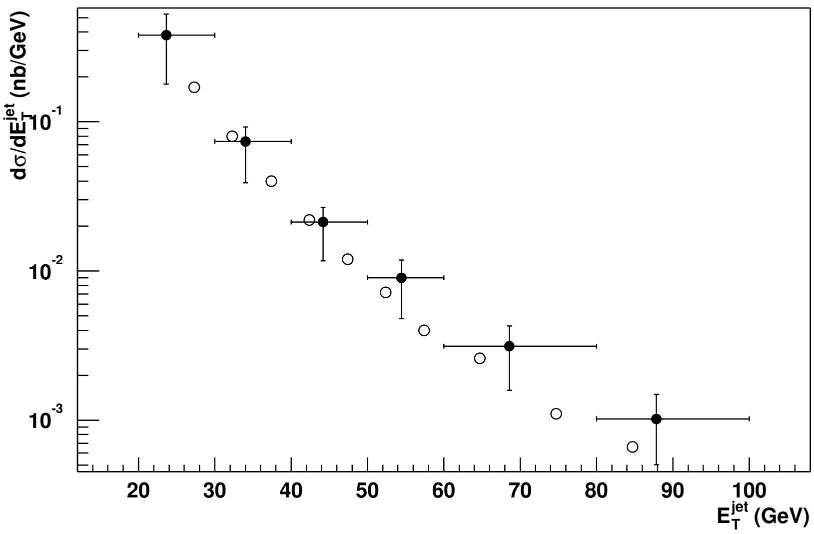

Figure 5.10: *B-jet cross section, with $B \rightarrow \mu$, as a function of unsmeared E_T^{jet}. Open circles represent the Run I measurement.*

5.2.1 Validity test of algorithm

The validity of the unfolding algorithm is tested using the Monte Carlo simulation, from which we can extract the spectra of both the unsmeared jets and the smeared jets. Unfolding the smeared jet spectrum using above algorithm has to result in the unsmeared jet spectrum. Figure 5.11 shows the smeared jet spectrum as it is extracted from the Monte Carlo simulation, with the smeared ansatz function represented by the solid line. Due to statistical limitations, only the bins between 20 and 80 GeV are taken into account in the fit. The corresponding underlying ansatz function is shown in figure 5.12, where it is compared with the unsmeared jet spectrum. Clearly the ansatz function and the unsmeared jet spectrum agree, validating the algorithm.

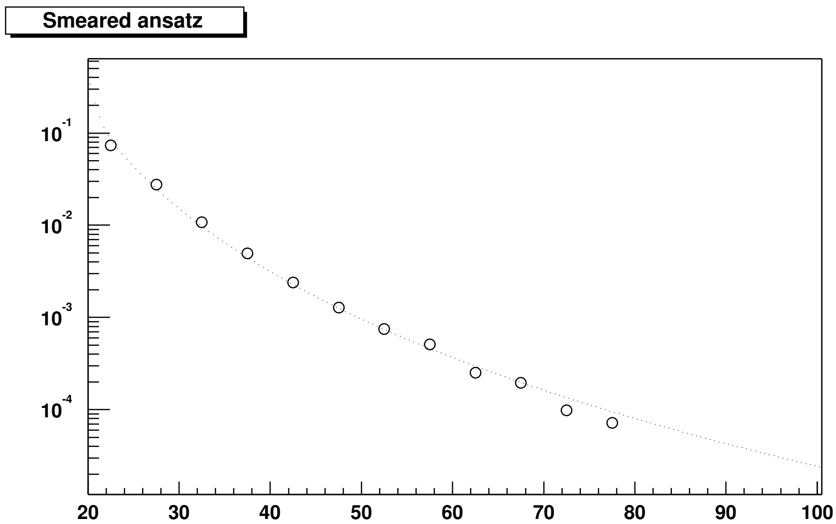

Figure 5.11: *Smeared ansatz function, represented by the dotted line, compared with the spectrum of smeared jets extracted from the Monte Carlo simulation.*

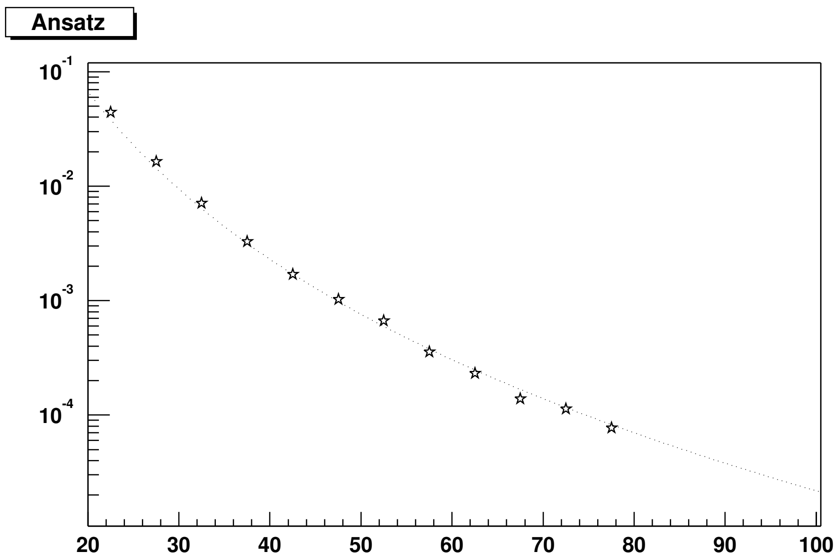

Figure 5.12: *Ansatz function, represented by the dotted line, compared with the spectrum of unsmeared jets extracted from the Monte Carlo simulation.*

5.2.2 Effect of unfolding the μ+jet cross section

In the previous section, we first folded the μ+jet cross section with the measured b-jet content, before proceeding with the unfolding algorithm. However, the b-jet content is dependent on E_T^{jet}, and changes the shape of the cross section. A good systematic check on this procedure is therefore to first unfold the μ+jet cross section before folding it with the b-jet content. The ratio between the smeared and unsmeared ansatz functions should be similar for the μ+jet cross section as for the b-jet cross section; any discrepancies have to be taken into account in the systematical error on the measurement. We use the same ansatz function as explained above to unfold the μ+jet cross section, using the same resolution function. Figure 5.13 shows the result of the unfolding procedure, with the data points on top of the smeared ansatz function (solid line) and the unsmeared ansatz function represented by the dotted line. Clearly the smeared ansatz function represents the data well. The ratio between the smeared and unsmeared ansatz function is shown in figure 5.14, with the error bands resulting from floating the error on the resolution function. As is shown in figure 5.15, the ratio for the μ+jet unfolding is compatible with the ratio measured for the b-jet unfolding, except for the higher E_T^{jet} bins. To take this into account, we increase the lower error on the b-jet unfolding ratio to the value of the μ+jet unfolding ratio. This slightly increases the high error of the b-jet cross section in the higher E_T^{jet} bins, as shown in figure 5.16.

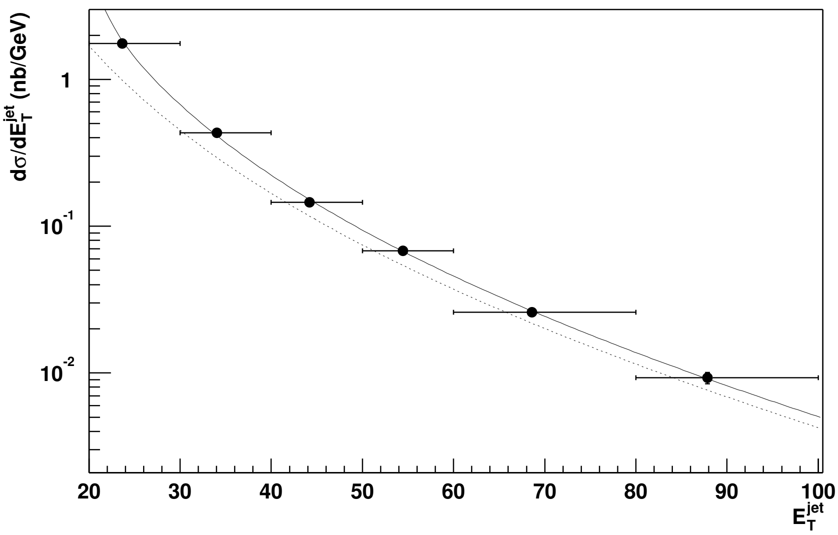

Figure 5.13: *Result of unfolding the μ+jet cross section. Smeared data points are represented by the black points, lying on top of the smeared ansatz function (solid line). The dotted line represents the ansatz function.*

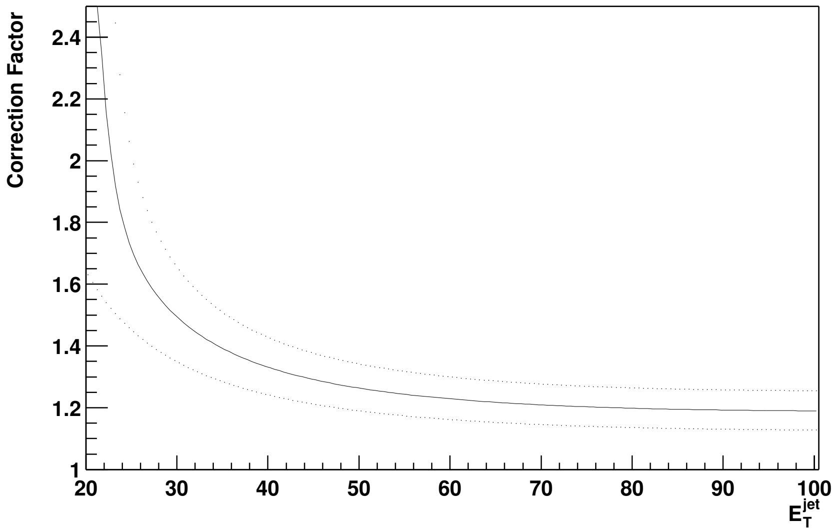

Figure 5.14: *Ratio between the smeared and unsmeared ansatz function for the μ+jet cross section*

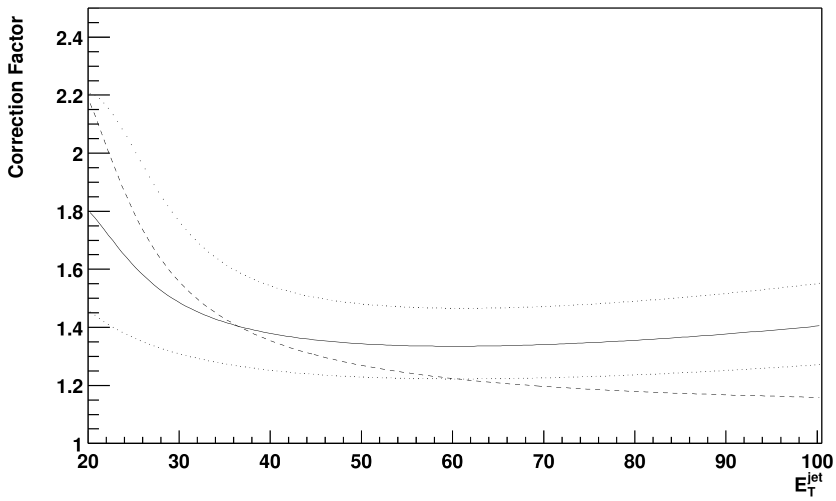

Figure 5.15: *Ratio between the smeared and unsmeared ansatz function for the b+jet cross section represented by the solid line, with the ratio for the μ+jet unfolding represented by the dashed line.*

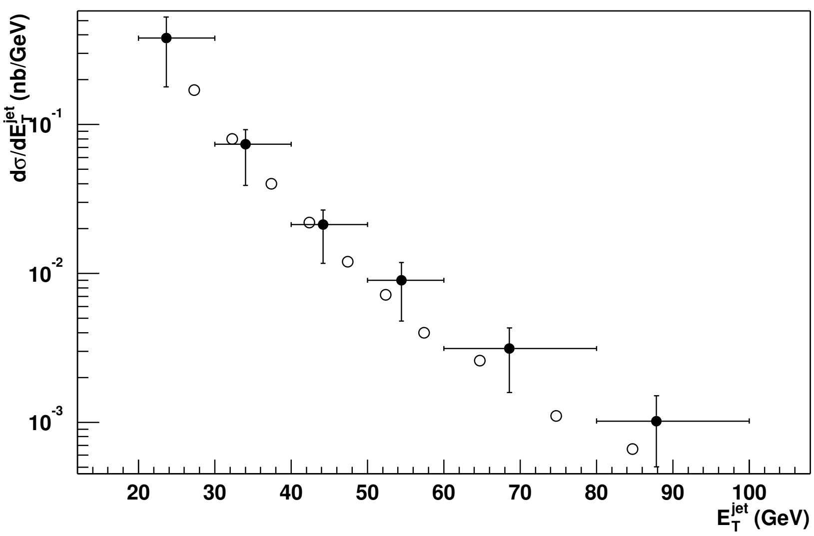

Figure 5.16: *Unsmeared b-jet cross section, with updated errors to account for additional errors coming from the μ+jet unfolding ratio.*

5.3 Acceptance corrections

In the previous section, we have derived the differential b-jet cross section, with the b-quark decaying to a muon. These cross sections do not take into account the tagging muon, except for the energy deposition of the muon in the calorimeter. Also, the cross section is measured in a limited η range. To extract the differential b-jet cross section from this measurement, which can be confronted with the theory, we need to correct the cross section according to:

$$\frac{d\sigma^{b-jet}}{dE_T^{jet}} = \frac{A(E_T)}{2BR} \frac{d\sigma^{\mu(b)-jet}}{dE_T^{jet}} \tag{5.4}$$

where $\frac{d\sigma^{b-jet}}{dE_T^{jet}}$ is the differential b-jet cross section, $A(E_T)$ is the acceptance of the detector, and BR is the $b \to \mu$ branching ratio. The factor $\frac{A(E_T)}{BR}$ is extracted from the Monte Carlo simulation. (note: currently I am working on this acceptance correction, but I don't have results yet.)